Noname manuscript No.
(will be inserted by the editor)

Numerical study of two-airfoil arrangements by a discrete vortex method

Thierry M. Faure · Laurent Dumas · Olivier Montagnier

Received: date / Accepted: date

Abstract The aerodynamic characteristics of two neighboring airfoils are greatly different from those of a single airfoil, both for attached or detached flows conditions. In order to study the features of a two-airfoil arrangement with variations in the angle of attack and distances between the airfoils, and considering possible flow detachments, an adaptation of a discrete-time vortex numerical method is conducted. It is based on the fact that for a given airfoil and Reynolds number, there is a critical value of the leading-edge suction parameter. If its instantaneous value exceeds the critical value, vortex shedding occurs at the leading edge, representing the shear layer associated with flow detachment. In addition, Kelvin's theorem imposes for each time step, that the total circulation equals zero. In the present paper, Kelvin's theorem is extended for a two-airfoil arrangement with the initial starting flow condition. That numerical method allows to obtain instantaneous flow features and airfoil forces for different arrangements. Validation of the method is made for unsteady motions of oscillating and plunging airfoils. For constant angle-of-attack airfoils, comparisons with available experimental data are presented in terms of flow field and aerodynamic coefficients. In particular, in order to show the possible improvement of the two-airfoil arrangement performance, the averaged lift coefficient is compared with the single airfoil configuration. A discussion on the lift efficiency ratio with previous measurements and time development of the flow field, permits to understand the mechanisms contributing to a positive interaction.

Thierry M. Faure · Laurent Dumas · Olivier Montagnier
Centre de Recherche de l'École de l'Air, École de l'Air, F-13661 Salon-de-Provence, France
e-mail: thierry.faure@ecole-air.fr

1 Introduction

Unsteady aerodynamics of airfoils in incompressible flow, operated on moderate Reynolds numbers in the range 10^4 to 10^5, has gained in importance, for unmanned air vehicles (UAV) and micro air vehicles (MAV) applications (Mueller and DeLaurier (2003)). Fixed-wing MAV need to fly at conditions close to the stall point, and post-stall flight would occur during maneuvers. Hence, delaying stall and improving performance for large values of the angle of attack is necessary. To do so, two-wing arrangements are proposed as a means of generating large enough lift coefficient and delaying stall by controlling the flow. The present investigation focuses on the understanding of two-dimensional effects using a discrete vortex method. The interaction between two airfoils is a key mechanism of flow control, with wakes and vortex shedding effects.

The first analytical method for the estimate of lift coefficient of a constant angle of attack, attached flow airfoil, is the thin airfoil theory developed by Munk (1922), Birnbaum (1923) and Glauert (1926). The unsteady solution for the lift of an airfoil undergoing a step change in angle of attack was solved by Wagner (1925). Theodorsen (1935) developed a potential flow solution for a flat plate oscillating in pitch and plunge with a small-amplitude harmonic motion. Unsteady aerodynamic theories and their applications to flapping or aeroelasticity of an airfoil have been established by Garrick (1937) and von Kármán and Sears (1938). These methods are valuable but are based on the potential theory, and their use is limited to fully attached flows. The adaptation of the thin airfoil theory to detached flows emerges in the 1970s with the advances of computer science, with relative limited power at that time. Clements (1973), Clements and Maull (1975) and Kiya and Arie (1977) introduced vortex shedding to model the flow behind a detached body. Kuwahara (1973) and Sarpkaya (1975) numerically studied the detached flow behind a flat plate using a vortex method and a conformal transform. The knowledge of the separation position on an airfoil allows Katz (1981) to adapt a discrete vortex method for a partially detached airfoil. The development of more powerful computers in this decade, leads flow simulation toward another way with the high-order resolution of Navier-Stokes equations with closure models, and approaches like Discrete Eddy Simulation (DES), Large Eddy Simulation (LES) or Direct Numerical Simulation (DNS). However, these approaches present heavy computing costs and require long simulation time. For this reason, discrete vortex methods came back in use recently as alternative low-order methods to classical high-order Computational Fluid Dynamics (CFD), to address engineering issues with relevant accuracy. A method for the prediction of continuous vortex shedding around a general sharp-edged solid body, moving in an inviscid fluid at Reynolds numbers between 100 and 1000 has been developed by Michelin and Smith (2009). Ansari et al. (2006), Wang and Eldredge (2013), Xia and Mohseni (2013) and Hammer et al. (2014) developed discrete vortex methods to model leading edge vortices in unsteady flows. However, these methods are limited to start and stop criteria for the vortex shedding. Ramesh et al. (2013b) and Ramesh et al. (2014) addressed this issue with the implementation of a leading edge suction parameter. That criterion allows a wide range of applications for any airfoil geometry, with sharp or rounded leading edges, and any arbitrary motion. It proves its robustness and its relative accuracy as long as a leading edge boundary layer separation occurs and is fully validated at Reynolds numbers of 3×10^4 and 10^5. The Leading-edge-suction-parameter Discrete Vortex Method (LDVM) algorithm is based, for each time step, on iterative schemes to obtain the amplitude of the last generated vortices through a converging time consuming process. A modified algorithm has been implemented by Faure et al. (2019), where the Newton-Raphson iteration search is replace by a linear system, providing a reduction of the simulation time by a factor of 2.

In the present paper, the modified version of the algorithm of Ramesh et al. (2013b) and Ramesh et al. (2014) and developed by Faure et al. (2019), is adapted to a two-airfoil arrangement where Kelvin's theorem is modified using the initial condition. That numerical method allows to obtain instantaneous flow features and forces for different airfoil arrangements. The validation is made for unsteady airfoil motions using the results of numerical simulations for tandem flapping wings (Broering and Lian (2012)) and experiments of an oscillating forefoil and a static hindfoil positioned in its wake (Rival et al. (2010)). The LDVM for a two-airfoil arrangement is then compared with available experimental data varying the angle of attack for a fixed distance beween the airfoils (Faure et al. (2017)) or for a stagger and gap defined relatively to the upstream flow direction (Jones et al. (2015)). In particular, the averaged lift coefficient of the two-airfoil arrangement is compared with the averaged lift coefficient of the single airfoil in order to show a possible improvement of the performance for particular parameters.

2 LDVM adaptation for a two-airfoil arrangement

The analysis of multiply-connected problems like the present one, has been extensively studied for attached flows (Crowdy and Marshall (2006), Crowdy et al. (2007), Crowdy and Surana (2007)). It permits the exact calculation of potential flows around multi-body configurations (Crowdy (2010)) using the multiply-connected Schwarz-Christoffel formula (Crowdy (2007), Crowdy (2008)).

The founding principles and calculation parameters of the leading edge suction parameter modulated discrete vortex method (LDVM) are similar to Ramesh et al. (2013b) and Ramesh et al. (2014). An airfoil is placed in an upstream flow of magnitude U_∞ with an angle of attack α, the aerodynamic frame of reference is (X, Z) with X the direction of U_∞ and Z perpendicular to X (figure 1). The velocity components in this frame are U and W. The airfoil frame of reference is (x, z) with x the chord-wise direction and z perpendicular to x, the velocity component normal to the airfoil is w. A plunging motion $\dot{h}$ of the airfoil along axis Z can be considered.

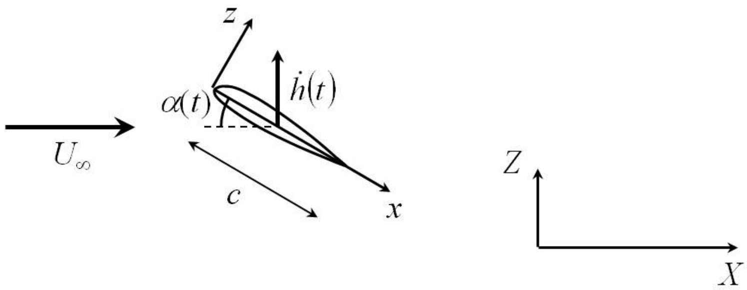

Fig. 1: Unsteady airfoil frame of reference (x, z) and aerodynamic frame of reference (X, Z).

For a two-airfoil arrangement and possible detached flow conditions, the LDVM needs to be adapted. In that case, the upstream airfoil, or forefoil, is referred as airfoil 1 and the downstream airfoil, or hindfoil, as airfoil 2. The wakes and shedding point vortices created by these airfoils, and the potential effects between them, modify the flow and the aerodynamic performance of the arrangement.

Each airfoil is modeled by a time-dependent vorticity distribution $\gamma_j(\theta, t)$ taken to be a Fourier series (Glauert (1926)), with $j = \{1, 2\}$:

$$\gamma_j(\theta, t) = 2U_\infty \left[A_{0,j}(t) \frac{1 + \cos\theta}{\sin\theta} + \sum_{n=1}^{\infty} A_{n,j}(t) \sin n\theta \right] \tag{1}$$

with, for each airfoil, the new variable θ resulting from the transformation of the chord-wise coordinate x such as:

$$x = \frac{c}{2}(1 - \cos\theta) \tag{2}$$

The time-dependent Fourier coefficients are obtained from the velocity field $w_j(t)$ by enforcing the boundary condition that the flow must remain tangential to the airfoil:

$$A_{0,j}(t) = -\frac{1}{\pi} \int_0^\pi \frac{w_j(\theta, t)}{U_\infty} d\theta \tag{3}$$

$$A_{n,j}(t) = \frac{2}{\pi} \int_0^\pi \frac{w_j(\theta, t)}{U_\infty} \cos n\theta d\theta \tag{4}$$

The induced velocity normal to each airfoil is calculated from motion kinematics (Katz and Plotkin (2001)), with $j = \{1, 2\}$, $k = \{1, 2\}$ and $k \neq j$:

$$
\begin{aligned}
w_j = \frac{\partial \eta_j}{\partial x} & \left[\frac{\partial \Phi_{TEV,j}}{\partial x} + \frac{\partial \Phi_{LEV,j}}{\partial x} + \frac{\partial \Phi_{TEV,k}}{\partial x} + \frac{\partial \Phi_{LEV,k}}{\partial x} + \frac{\partial \Phi_{B,k}}{\partial x} \right. \\
& \left. + U_\infty \cos\alpha + \dot{h}_j \sin\alpha \right] - \frac{\partial \Phi_{TEV,j}}{\partial z} - \frac{\partial \Phi_{LEV,j}}{\partial z} \\
& - \frac{\partial \Phi_{TEV,k}}{\partial z} - \frac{\partial \Phi_{LEV,k}}{\partial z} - \frac{\partial \Phi_{B,k}}{\partial z} - U_\infty \sin\alpha \\
& - \dot{\alpha}_j \left(x - x_{p,j} \right) + \dot{h}_j \cos\alpha
\end{aligned}
\tag{5}
$$

where $\Phi_{LEV,j}, \Phi_{LEV,k}$ and $\Phi_{TEV,j}, \Phi_{TEV,k}$ are the velocity potentials associated to leading edge and trailing edge vortices (LEV and TEV), $\Phi_{B,k}$ is the velocity potential associated to vorticity distribution along the kth airfoil, η_j the airfoil camber-line, $x_{p,j}$ the pivot location, $\dot{\alpha}_j$ the time derivative of the angle of attack corresponding to a pitch motion of the jth airfoil and $\dot{h}_j$ its velocity along Z, corresponding to a plunge. The airfoil bound circulation is calculated by integrating the chord-wise distribution of vorticity over the airfoil:

$$
\Gamma_{B,j}(t) = U_\infty c \pi \left[A_{0,j}(t) + \frac{A_{1,j}(t)}{2} \right] \tag{6}
$$

For each airfoil, the leading edge suction parameter (LESP) is a non-dimensional measure of the suction at the leading edge (Garrick (1937)) which is equal to the first Fourier coefficient of the vorticity distribution (Ramesh et al. (2014)), with $j = \{1, 2\}$:

$$
\mathrm{LESP}_j(t) = A_{0,j}(t) \tag{7}
$$

The critical value $\mathrm{LESP}_{crit,j}$ is a measure of the maximum suction that a given airfoil can bear before separation and is independent of its motion (Ramesh et al. (2011), Ramesh (2013), Ramesh et al. (2018)). Beyond the value $\mathrm{LESP}_{crit,j}$, the airfoil suction side boundary layer separates from the leading edge, which corresponds to the release of a leading edge vortex. If LESP_j becomes lower than its critical value, LEV shedding is stopped. Then, the LESP concept is a single empirical parameter governing the wall viscous effect and boundary layer detachment.

Non-dimensional variables are introduced:

$$
\begin{gathered}
w^* = \frac{w}{U_\infty} \qquad U^* = \frac{U}{U_\infty} \qquad W^* = \frac{W}{U_\infty} \qquad X^* = \frac{X}{c} \qquad Z^* = \frac{Z}{c} \\
\Gamma^* = \frac{\Gamma}{U_\infty c} \qquad \eta^* = \frac{\eta}{c} \qquad \dot{h}^* = \frac{\dot{h}}{U_\infty} \qquad \dot{\alpha}^* = \frac{d\alpha}{dt^*}
\end{gathered}
\tag{8}
$$

The velocity induced by the kth vortex is described with the model of Vatistas et al. (1991) which considers a finite core radius r_c with a solid-body rotation:

$$
\begin{aligned}
U_k^* &= \frac{\Gamma_k^*}{2\pi} \frac{Z^* - Z_k^*}{\sqrt{\left[\left(X^* - X_k^*\right)^2 + \left(Z^* - Z_k^*\right)^2\right]^2 + r_c^{*4}}} \\
W_k^* &= -\frac{\Gamma_k^*}{2\pi} \frac{X^* - X_k^*}{\sqrt{\left[\left(X^* - X_k^*\right)^2 + \left(Z^* - Z_k^*\right)^2\right]^2 + r_c^{*4}}}
\end{aligned}
\tag{9}
$$

with:

$$
r_c^* = \frac{r_c}{c} \tag{10}
$$

The non-dimensional time step is the same as the one used by Ramesh et al. (2014):

$$
\delta t^* = \frac{\delta t U_\infty}{c} = 0.015 \tag{11}
$$

The vortex core radius is taken to be 1.3 times the average spacing between vortices as proposed by Leonard (1980):

$$
r_c^* = \frac{r_c}{c} = 1.3\delta t^* = 0.02 \tag{12}
$$

The location of the new ith vortex is approximated by drawing a vector from the shedding edge to the previous shed vortex and taking the position at one-third this distance (Ansari et al. (2006)), for instance for the TEV and the jth airfoil:

$$
\begin{aligned}
X_{TEV,j,i}^* &= X_{TE,j}^* + \frac{1}{3}\left(X_{TEV,j,i-1}^* - X_{TE,j}^*\right) \\
Z_{TEV,j,i}^* &= Z_{TE,j}^* + \frac{1}{3}\left(Z_{TEV,j,i-1}^* - Z_{TE,j}^*\right)
\end{aligned}
\tag{13}
$$

where $X_{TE,j}^*, Z_{TE,j}^*$ are the trailing edge coordinates of the jth airfoil in the aerodynamic frame of reference. The advantage of the current approach is that account is taken not only of the possible wing motion since the last time-step but also of the advection of the previous shed vortex, giving overall a more accurate depiction of the flow.

Consider a time step i where LEV and TEV are emitted from both airfoils. The velocity component tangential to the upstream and downstream airfoils are, with $j = \{1,2\}$, $k = \{1,2\}$ and $k \neq j$:

$$
\begin{aligned}
w_j^*(\theta) = T_j(\theta) + \textstyle\sum_{l=1}^{2} &\left[\Gamma_{TEV,l,i}^* T_{j,l,TEV,i}(\theta) + \Gamma_{LEV,l,i}^* T_{j,l,LEV,i}(\theta)\right] \\
&+ \Gamma_{B,k}^* T_{B,k}(\theta)
\end{aligned}
\tag{14}
$$

the coefficients are respectively, with $j = \{1, 2\}$:

$$\begin{array}{rl} T_j(\theta) = & \left[\left(\sum_{l=1}^{i-1} U^*_{TEV,j,l} + \sum_{m=1}^{i-1} U^*_{LEV,j,m} + 1\right)\cos\alpha \right. \\ & \left. - \left(\sum_{l=1}^{i-1} W^*_{TEV,j,l} + \sum_{m=1}^{i-1} W^*_{LEV,j,m}\right)\sin\alpha\right] \dfrac{\partial \eta_j^*}{\partial x^*} \\ & - \sin\alpha - \dot{\alpha}^*\left(x_j^* - x_{j,p}^*\right) + \dot{h_j}^* \cos\alpha \\ & - \sum_{l=1}^{i-1} W^*_{TEV,j,l}\cos\alpha + \sum_{m=1}^{i-1} U^*_{LEV,j,m}\sin\alpha \end{array} \tag{15}$$

with for $j = \{1, 2\}$ and $l = \{1, 2\}$:

$$\begin{array}{rl} T_{j,l,TEV,i}(\theta) = & U^*_{TEV,l,i}\left(\dfrac{\partial \eta_j}{\partial x}\cos\alpha - \sin\alpha\right) \\ & + W^*_{TEV,l,i}\left(-\cos\alpha - \dfrac{\partial \eta_j}{\partial x}\sin\alpha\right) \\ T_{j,l,LEV,i}(\theta) = & U^*_{LEV,l,i}\left(\dfrac{\partial \eta_j}{\partial x}\cos\alpha - \sin\alpha\right) \\ & + W^*_{LEV,l,i}\left(-\cos\alpha - \dfrac{\partial \eta_j}{\partial x}\sin\alpha\right) \end{array} \tag{16}$$

and for $j = \{1, 2\}$, $k = \{1, 2\}$ and $k \neq j$:

$$\begin{array}{rl} T_{B,k}(\theta) = & U^*_{B,k}\left(\dfrac{\partial \eta_j}{\partial x}\cos\alpha - \sin\alpha\right) \\ & + W^*_{B,k}\left(-\cos\alpha - \dfrac{\partial \eta_j}{\partial x}\sin\alpha\right) \end{array} \tag{17}$$

The bound circulation for each airfoil,with $j = \{1, 2\}$, $k = \{1, 2\}$ and $k \neq j$, is given by:

$$\begin{array}{rl} \mathit{\Gamma}^*_{B,j} & = \int_0^\pi w_j^*(\theta)(\cos\theta - 1)\, d\theta \\ & = I_j + \mathit{\Gamma}^*_{TEV,j,i} I_{j,j,TEV} + \mathit{\Gamma}^*_{LEV,j,i} I_{jjj,LEV} \\ & + \mathit{\Gamma}^*_{TEV,k,i} I_{j,k,TEV} + \mathit{\Gamma}^*_{LEV,k,i} I_{j,k,LEV} + \mathit{\Gamma}^*_{B,k} I_{B,k} \end{array} \tag{18}$$

with the coefficients, for $j = \{1, 2\}$, $k = \{1, 2\}$ and $k \neq j$:

$$\begin{array}{rl} I_j & = \int_0^\pi T_j(\theta)(\cos\theta - 1)\, d\theta \\ I_{j,k,TEV} & = \int_0^\pi T_{j,k,TEV}(\theta)(\cos\theta - 1)\, d\theta \\ I_{j,k,LEV} & = \int_0^\pi T_{j,k,LEV}(\theta)(\cos\theta - 1)\, d\theta \\ I_{B,k} & = \int_0^\pi T_{B,k}(\theta)(\cos\theta - 1)\, d\theta \end{array} \tag{19}$$

The first Glauert coefficient for each airfoil, with $j = \{1, 2\}$, $k = \{1, 2\}$ and $k \neq j$, is then:

$$\begin{array}{rl} A_{0,j} & = -\frac{1}{\pi}\int_0^\pi w_j^*(\theta)\, d\theta \\ & = J_j + \mathit{\Gamma}^*_{TEV,j,i} J_{j,j,TEV} + \mathit{\Gamma}^*_{LEV,j,i} J_{j,j,LEV} \\ & + \mathit{\Gamma}^*_{TEV,k,i} J_{j,k,TEV} + \mathit{\Gamma}^*_{LEV,k,i} J_{j,k,LEV} + \mathit{\Gamma}^*_{B,k} J_{B,k} \end{array} \tag{20}$$

with for $j = \{1, 2\}$, $k = \{1, 2\}$ and $k \neq j$:

$$\begin{aligned} J_j &= -\frac{1}{\pi}\int_0^\pi T_j\left(\theta\right)d\theta \\ J_{j,k,TEV} &= -\frac{1}{\pi}\int_0^\pi T_{j,k,TEV}\left(\theta\right)d\theta \\ J_{j,k,LEV} &= -\frac{1}{\pi}\int_0^\pi T_{j,k,LEV}\left(\theta\right)d\theta \\ J_{B,k} &= -\frac{1}{\pi}\int_0^\pi T_{B,k}\left(\theta\right)d\theta \end{aligned} \tag{21}$$

Comparing the LDVM algorithm with the single-airfoil arrangement, for each time step, circulations associated to the TEV and LEV are created for the second airfoil, providing one or two new variables, depending on if the flow is detached or attached. If both airfoils are detached, there are four unknown new variables at each time step. The available equations are the LESP criteria for airfoil 1 and 2 and Kelvin's theorem, meaning three equations for four unknown parameters:

$$A_{0,1} - \mathrm{LESP}_{crit,1} = 0 \tag{22}$$

$$A_{0,2} - \mathrm{LESP}_{crit,2} = 0 \tag{23}$$

$$\begin{aligned} \Gamma^*_{B,1} + \Gamma^*_{B,2} + \Gamma^*_{TEV,1,i} + \Gamma^*_{LEV,1,i} + \Gamma^*_{TEV,2,i} + \Gamma^*_{LEV,2,i} \\ + \textstyle\sum_{k=1}^{i-1}\Gamma^*_{TEV,1,k} + \sum_{l=1}^{i-1}\Gamma^*_{LEV,1,l} \\ + \textstyle\sum_{m=1}^{i-1}\Gamma^*_{TEV,2,m} + \sum_{n=1}^{i-1}\Gamma^*_{LEV,2,n} = 0 \end{aligned} \tag{24}$$

where the indices 1 and 2 are relative to airfoils 1 and 2. There is scant literature on the treatment of Kelvin's circulation theorem for multiple airfoils. This issue has been addressed by Lighthill in the treatment of the Weis-Fogh mechanism developed for hovering animal flight (Weis-Fogh (1973), Lighthill (1973)).

To close the problem, an additional condition is necessary. As LDVM simulations are starting with airfoils at rest, the initial condition is used, which is the circulation around contours C_1 and C_2 including each airfoil equals zero (figure 2a), resulting in a division in two parts of Kelvin's equation (24). Since the circulation around the time development of a given contour, made of the same fluid elements, is kept for the following times (figure 2b), equation (24) of the previous system is replaced by:

$$\Gamma^*_{B,1} + \Gamma^*_{TEV,1,i} + \Gamma^*_{LEV,1,i} + \sum_{k=1}^{i-1}\Gamma^*_{TEV,1,k} + \sum_{l=1}^{i-1}\Gamma^*_{LEV,1,l} = 0 \tag{25}$$

$$\Gamma^*_{B,2} + \Gamma^*_{TEV,2,i} + \Gamma^*_{LEV,2,i} + \sum_{m=1}^{i-1}\Gamma^*_{TEV,2,m} + \sum_{n=1}^{i-1}\Gamma^*_{LEV,2,n} = 0 \tag{26}$$

Thus, the circulation generation is decoupled from airfoils 1 and 2 in the two-airfoil arrangement by the initial condition, but the global flow and the advection of the point vortices are calculated with all the circulations present at a given time. The continuously deforming contours could present quite exotic shapes, but point vortices are generally organized in clusters. Figure 2b is idealized, since a vortex cluster generated from airfoil 1 can be advected in the vicinity of airfoil 2. Then, this vortex cluster has a strong influence on the velocity w_2 normal to this second airfoil in the calculation of the coefficient $A_{0,2}$, but is considered in Kelvin's theorem only for its originating airfoil 1, in equation (25). In order to prevent a point vortex originating from airfoil 1 crossing the camber-line of airfoil 2, a condition avoiding this case has been implemented. This condition also avoids contour C_1 to cross airfoil 2 camber line.

The linear system of four unknown parameters for four equations is solved without iterative scheme. The resolution of this linear system is then performed in the same way as for a single airfoil (Faure et al. (2019)), without any Newton-Raphson iterative scheme as in the initial LDVM algorithm (Ramesh et al. (2014)). The velocity field used for the advection is obtained considering the influence of the bound airfoil circulations and all the shed vortices.

One of the main drawbacks of discrete vortex methods is the increase of computing time as the square of the number n of shedding centers, $O\left(n^2\right)$. In order to decrease this computing time and keep the advantages of low-order models, it is necessary to reduce the number of point vortices without altering much the flow description. A deletion of the centers that exit the field of interest could be employed, but Kelvin's circulation theorem is not enforced anymore for each time step, resulting in sharp peaks changes in the time development of the aerodynamic coefficients. Another option is a model reduction based on a point vortex concentration. Point vortex shedding from the leading edge is modeled by a shear layer that comprises few discrete point vortices, concentrated in a single point vortex whose strength varies with time (Suresh-Babu et al. (2016)). Fast summation methods are alternative options to reduce the computation time to $O\left(n \log n\right)$ (Barnes and Hut (1986)) or to $O\left(n\right)$ (Carrier et al. (1988)). Such methods, proposed first by Sarpkaya (1975), consist in a clustering of all the individual vortex centers situated downstream of a given distance downstream from the airfoil. It presents the advantage of not altering much the vortices near the airfoil, whose contribution is more important to aerodynamic forces, and to conserve the global circulation null. Recently, an aggregation procedure has been developed and utilized, in which vortex elements are coalesced at each time step, whatever their relative distance from the airfoil (Darakananda et al. (2018), Darakananda and Eldredge (2019)).

However, the way the distant point vortices are removed or coalesced into an equivalent single point vortex is a relevant issue. In the present study, an automatic vortex clustering method based on a k-d tree of neighboring vortices is adopted (Bentley (1975)), as proposed in Faure et al. (2019), only for point vortices located four chords downstream of the aft airfoil. For the agglomeration of point vortices, several methods have been tested to travel across the tree in search for the neighbors. The most efficient method is to start with the closest point vortices from the airfoil. Note that the method only takes into account the distances between point vortices. Their values are used to compute the barycenter of the equivalent vortex center. Once merged, the sum of the circulations of the clustered point vortices is assigned to the new point vortex.

Note that the vortex amalgamation procedure is realized four chord downstream of airfoil 2, which is a distance sufficient to avoid any noticeable influence on the forces coefficients exerted on this airfoil (Faure et al. (2019)). In addition, that procedure does not violate Kelvin's theorem for each airfoil, even if two vortices, originating from different airfoils, are merged together. For instance, if a point vortex $\Gamma^*_{LEV,1,m}$ created at time step m from airfoil 1 is merged with a point vortex $\Gamma^*_{LEV,2,n}$ created at time step n from airfoil 2, the sum of their circulations $\Gamma^*_{LEV,1,m} + \Gamma^*_{LEV,2,n}$ is affected to their barycenter. However, in Kelvin's theorem for each airfoil, $\Gamma^*_{LEV,1,m}$ is always in equation (25) in the sum $\sum_{k=1}^{i-1} \Gamma^*_{LEV,1,k}$ while $\Gamma^*_{LEV,2,n}$ is always in equation (26) in the sum $\sum_{l=1}^{i-1} \Gamma^*_{LEV,1,l}$. In fact, as the algorithm is time-step developing, it is sufficient to keep the value of the sum of point vortices of previous step in both equations.

A direct resolution of the linear system (equations (22), (23), (25), (26)) provides circulations $\Gamma^*_{TEV,j,i}$, $\Gamma^*_{LEV,j,i}$ without any Newton-Raphson iterative loop as in Ramesh et al. (2014). In addition, a condition to avoid the traversing of the camber-line by a vortex has been added to the initial LDVM. Note that for a single airfoil arrangement, this change is marginal since very few vortices are following this path. However, that condition is important for a two-airfoil arrangement, if vortices are shedding from airfoil 1 on airfoil 2. Furthermore, as each airfoil is modelled by a vortex line, extending from its leading edge to its trailing edge, if a point vortex is advected by the flow and impacts the geometrical leading edge, it would be repealed or deviated because of the additional condition avoiding shedding vortices crossing airfoils camber-lines. A shedding cluster of point vortices can be advected toward the aft airfoil leading edge, even if none of the point vortices is exactly positioned on the leading edge. Two neighbor point vortices will repeal or attract each other, depending on their circulation, but never melt, unless a clustering is imposed by the algorithm for vortices located far away from the airfoils.

The aerodynamic normal and axial forces are obtained from the Fourier coefficients (Ramesh et al. (2014)) with $j = \{1, 2\}$, $k = \{1, 2\}$ and $k \neq j$:

$$
\begin{aligned}
F_{N,j} = \rho U_\infty c\pi \Bigg\{ & \left(U_\infty \cos\alpha + \dot{h}_j \sin\alpha\right) \left(A_{0,j} + \frac{A_{1,j}}{2}\right) \\
& + c\left(\frac{3\dot{A}_{0,j}}{4} + \frac{\dot{A}_{1,j}}{4} + \frac{\dot{A}_{2,j}}{8}\right) \\
& + \rho \int_0^c \left[\left(\frac{\partial \Phi_{TEV,j}}{\partial x}\right) + \left(\frac{\partial \Phi_{LEV,j}}{\partial x}\right) \right. \\
& \left. + \left(\frac{\partial \Phi_{TEV,k}}{\partial x}\right) + \left(\frac{\partial \Phi_{LEV,k}}{\partial x}\right) \right] \gamma_j(x,t)\, dx \Bigg\}
\end{aligned}
\tag{27}
$$

$$
F_{A,j} = \rho \pi c U_\infty^2 A_{0,j}^2 \tag{28}
$$

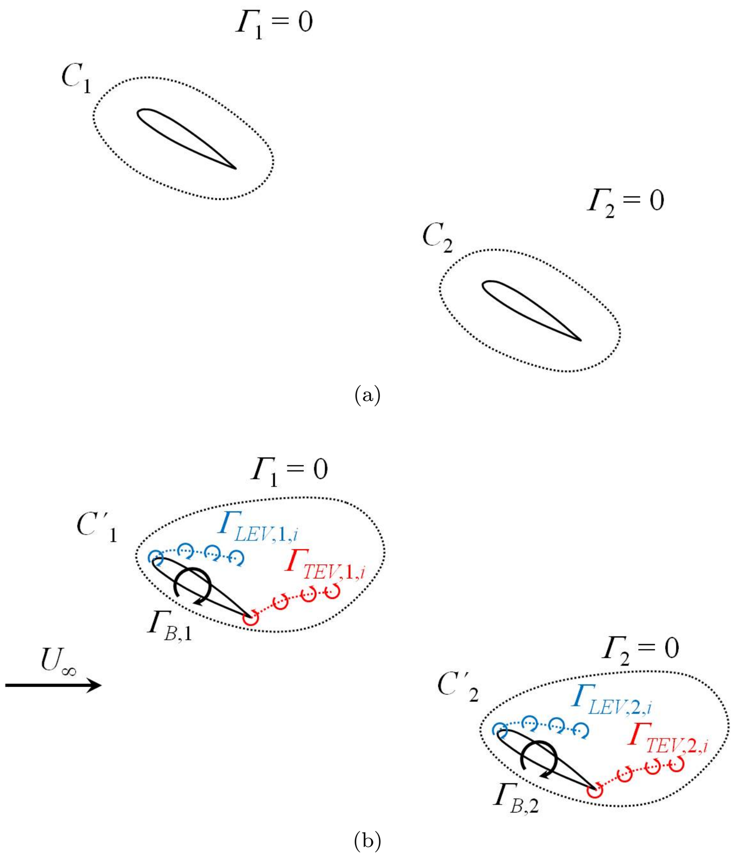

Fig. 2: Kelvin's theorem for a two-airfoil arrangement: (a) initial condition $t = 0$ at rest and circulation around contours C_1 and C_2, (b) once the upstream flow is established, conservation of circulations around the evolution C'_1 and C'_2 of contours C_1 and C_2 for $t > 0$.

The lift and drag forces are obtained by:

$$\begin{aligned} L_j &= F_{N,j} \cos\alpha + F_{A,j} \sin\alpha \\ D_j &= F_{N,j} \sin\alpha - F_{A,j} \cos\alpha \end{aligned} \tag{29}$$

Similarly for the pitching moment coefficient from the position $x_{ref,j}$:

$$
\begin{aligned}
M_j = x_{ref,j}F_{N,j} - \rho\pi c^2 U_\infty \Bigg\{ & \left(U_\infty \cos\alpha + \dot{h}_j \sin\alpha\right)\left(\frac{A_{0,j}}{4}\right. \\
& \left. + \frac{A_{1,j}}{4} - \frac{A_{2,j}}{8}\right) + c\left(\frac{7\dot{A}_{0,j}}{16} + \frac{3\dot{A}_{1,j}}{16} + \frac{\dot{A}_{2,j}}{16} - \frac{\dot{A}_{3,j}}{64}\right) \\
& -\rho \int_0^c \left[\left(\frac{\partial\Phi_{TEV,j}}{\partial x}\right) + \left(\frac{\partial\Phi_{LEV,j}}{\partial x}\right) + \left(\frac{\partial\Phi_{TEV,k}}{\partial x}\right)\right. \\
& \left. + \left(\frac{\partial\Phi_{LEV,k}}{\partial x}\right)\right] \gamma_j\left(x,t\right) x dx \Bigg\}
\end{aligned}
\tag{30}
$$

3 Validation of the two-airfoil LDVM for unsteady motions

For a single airfoil, the LDVM has been extensively compared with available data in Ramesh et al. (2014) and Faure et al. (2019), for both steady or moving airfoils. The two-airfoil LDVM is compared to CFD simulations of Broering and Lian (2012) for flapping tandem flat plates at a Reynolds number of 5000 and to measurements by particle image velocimetry (PIV) of Rival et al. (2010) for a SD7003 airfoil flapping in front of a downstream airfoil at a Reynolds number of $30,000$.

3.1 Tandem flapping wings

The flapping kinematics used in these CFD for two airfoils of equal chord c is a combination of sinusoidal pitching and plunging (Broering and Lian (2012)), with the pitch axis at the quarter-chord from each airfoil leading edge:

$$
\begin{aligned}
&\alpha\left(t\right) = \alpha_0 \cos\left(2\pi f t + \phi_\alpha + \phi_h\right) + \alpha_{ave} \\
&h\left(t\right) = h_0 \cos\left(2\pi f t + \phi_h\right)
\end{aligned}
\tag{31}
$$

where $\alpha\left(t\right)$ is the pitching angle, $h\left(t\right)$ the plunging position, t the time, $f = 1/T = 0.3$ Hz the flapping frequency, $\alpha_0 = 20°$ the pitching amplitude, $h_0 = 0.5c$ the plunging amplitude, $\phi_\alpha = 90°$ the pitching phase, ϕ_h the plunging phase, and $\alpha_{ave} = 5°$ the average angle of attack. In the present case, $\phi_h = 0°$ for the forefoil and 90° for the hindfoil. The Reynolds number based on the chord of each airfoil is 5000. This motion and Reynolds number are inspired from a dragonfly kinematics with a combination of pitching and plunging, on a tandem airfoil configuration. Figure 3 presents the flow and vortex generation for different spacings $\Delta X^* = \Delta X/c$ between 0.1 and 1, at 68% cycle time. The distance between the airfoils affect the timing of the vortex interactions. During the upstroke, the hindfoil passes through a TEV of the forefoil. Figure 4 presents the vortices at 89% cycle time just before stroke reversal and after the vortex interaction has occurred. A LEV with negative circulation is formed on the lower side of the hindfoil. Comparisons between the vorticity obtained from CFD (first row) and the circulation centers from LDVM (second row) are very similar for the forefoil downstroke ($t/T = 0.68$) as well as for the

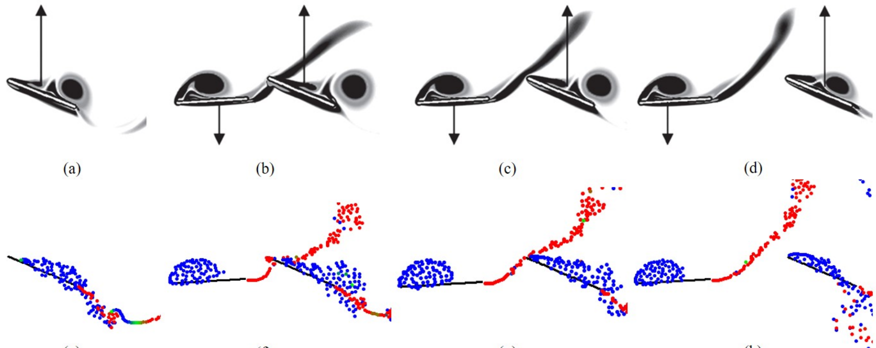

Fig. 3: Comparison between CFD from Broering and Lian (2012) (first row, vorticity, arrows indicate the stroke direction) and present LDVM (second row, circulation negative in blue, close to 0 in green and positive in red) at 68% cycle time for different spacings: (a) CFD single airfoil, (b) CFD tandem airfoil, spacing 0.25, (c) CFD tandem airfoil, spacing 0.5, (d) CFD tandem airfoil, spacing 1, (e) LDVM single airfoil, (f) LDVM tandem airfoil, spacing 0.25, (g) LDVM tandem airfoil, spacing 0.5, (h) LDVM tandem airfoil, spacing 1.

upstroke ($t/T = 0.89$). Figure 5 presents the comparison between CFD and LDVM for a period of flapping and different spacings $\varDelta X^* = \varDelta X/c$ between 0.1 and 1. A relatively good agreement is found between CFD and LDVM with similar shapes for the variation of lift and drag coefficients over a period. The accordance is excellent for a spacing of 1, but for lower spacings some discrepancies are observed between CFD and LDVM, with larger peak values for the LDVM.

3.2 Oscillating forefoil and static hindfoil

An experiment consisting on an oscillating forefoil and a static hindfoil positioned at $x/c = 2$ in its wake is realized with PIV measurements (Rival et al. (2010)). This configuration is referred to as a wave propeller developped by Schmidt and conceived to extract vortical energy from the forefoil to generate thrust on the hindfoil (Schmidt (1965)). Both foils are SD7003 airfoils which demonstrate relatively good performance at transitional Reynolds numbers. The forefoil plunging motion is a simple harmonic motion:

$$h\,(t) = h_0 \cos\,(2\pi f t) \tag{32}$$

where $h\,(t)$ is the plunging position, $h_0 = 0.5c$ the plunging amplitude and $f = 1/T = 2.5$ Hz the frequency. The forefoil angle of attack is 8°. The hindfoil is placed with a spacing of one chord downstream of the forefoil

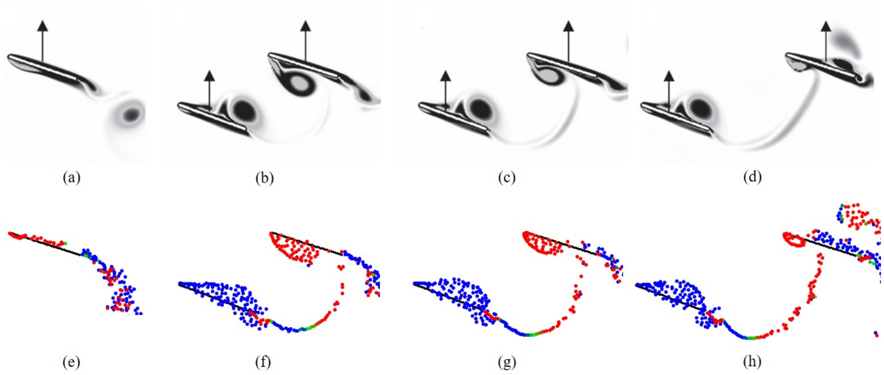

Fig. 4: Comparison between CFD from Broering and Lian (2012) (first row, vorticity, arrows indicate the stroke direction) and present LDVM (second row, circulation negative in blue, close to 0 in green and positive in red) at 89% cycle time for different spacings: (a) CFD single airfoil, (b) CFD tandem airfoil, spacing 0.25, (c) CFD tandem airfoil, spacing 0.5, (d) CFD tandem airfoil, spacing 1, (e) LDVM single airfoil, (f) LDVM tandem airfoil, spacing 0.25, (g) LDVM tandem airfoil, spacing 0.5, (h) LDVM tandem airfoil, spacing 1.

trailing edge, with a vertical offset $h^* = h/c = 0.5$ and an angle of attack of $8°$. The Reynolds number based on the chord of each airfoil is $30,000$. Forces are obtained from Particle Image Velocimetry (PIV) measurements by a control volume analysis, which allows time resolution decomposing a period of the forefoil into 12 phases per cycle. Figure 6 presents the comparison between vorticity measured from PIV fields and LDVM simulations for three different relative times of the forefoil cycle. Note in PIV fields that there is no velocity measurements in the airfoil pressure side because this region is a shadow zone of the PIV laser. For $t/T = 0.417$ a first forefoil LEV ejected downstream passes close over the hinfoil pressure side, and creates a leading edge separation identified in the LDVM field (figure 6b) but not in the PIV because this region is masked (figure 6a). As the hindfoil is near its stall angle, a vortex-induced separation occurs when the forefoil TEV passes close over the hindfoil leading edge (figure 6c and 6d). The forefoil flow is attached but the LEV and TEV previously generated are advected over the hindfoil (figures 6e and 6f). A good agreement is observed between flow features of vorticity fields measured by PIV and clusters of vortical centers obtained from LDVM. Figure 7 presents, for a period of the forefoil flapping, the comparison between PIV and LDVM for the global lift $C_{L,G}$ and drag $C_{D,G}$ coefficients:

$$\begin{aligned} C_{L,G} &= C_{L,fore} + C_{L,hind} \\ C_{D,G} &= C_{D,fore} + C_{D,hind} \end{aligned} \tag{33}$$

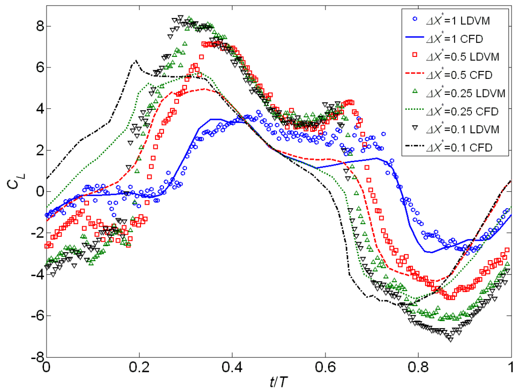

(a)

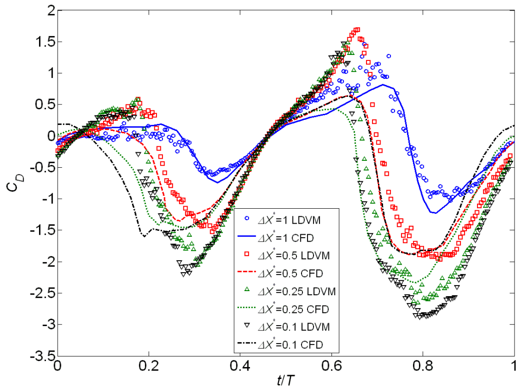

(b)

Fig. 5: Comparison between CFD and LDVM for the tandem flat plates kinematics and various spacings ΔX^* between 0.1 and 1: (a) lift coefficent, (b) drag coefficient.

where $C_{L,fore}$ and $C_{D,fore}$ are the forefoil coefficients and $C_{L,hind}$ and $C_{D,hind}$ the hindfoil coefficients. A relative agreement is found between the measurements and LDVM, since the force estimate by the control volume analysis does not consider the airfoil pressure side flow, which is a masked zone in the PIV velocity fields.

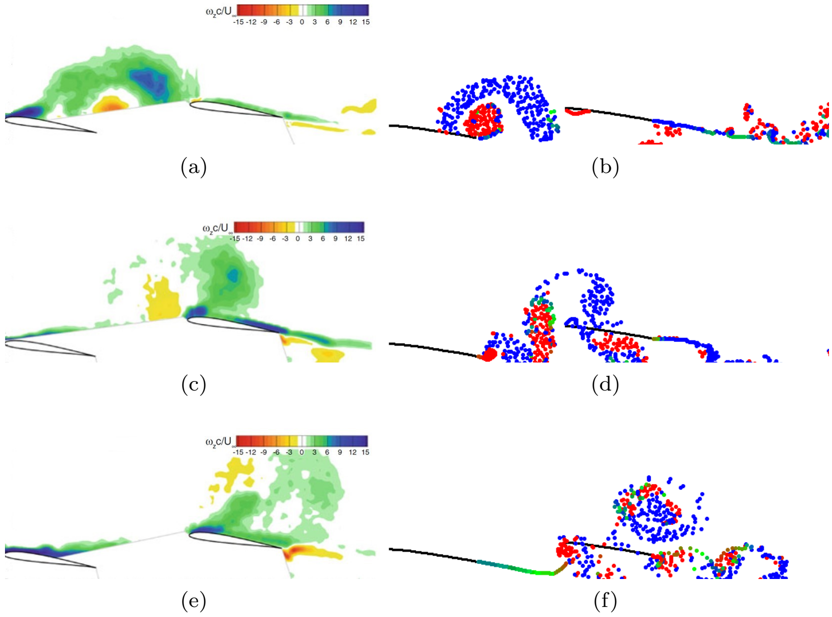

Fig. 6: Comparison of blade-vortex interaction for $h/c = -0.5$ and $\alpha_H = 8°$ from experiments of Rival et al. (2010) (left column) and LDVM (right column): (a) experiment $t/T = 0.417$, (b) LDVM $t/T = 0.417$, (c) experiment $t/T = 0.5$, (d) LDVM $t/T = 0.5$, (e) experiment $t/T = 0.583$, (f) LDVM $t/T = 0.583$.

4 LDVM for static two-airfoil arrangement

4.1 Fixed distance in the two-airfoil arrangement

A static two-airfoil arrangement is considered hereafter. In this section, for comparison with experimental data (Faure et al. (2017)), the distances (ℓ_x,ℓ_z) are counted in the airfoil frame of reference (x, z) with the chord of airfoil 2 half the chord c of airfoil 1 (figure 8). The distance between the forefoil trailing edge and the hindfoil leading edge is constant when the angle of attack is changed.

LDVM simulations flow fields are compared with PIV measurements of Faure et al. (2017) in figure 9, showing the vortex shedding for a given time for a Reynolds number $Re = 5.83 \times 10^4$ and distances $\ell_x/c = 3$ and $\ell_z/c = 1$. For experiments, where the flow is three-dimensional (figures 9a and 9b), the quantity obtained from PIV velocity fields is the Γ_2 criterion (negative in blue and positive in red) which is a normalized kinetic moment useful to identify vortical structures (Graftieaux et al. (2001)). The gray region below each air-

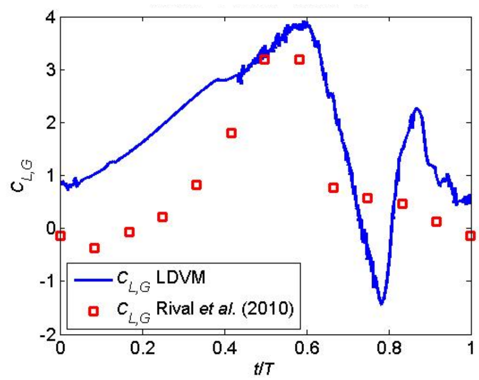

(a)

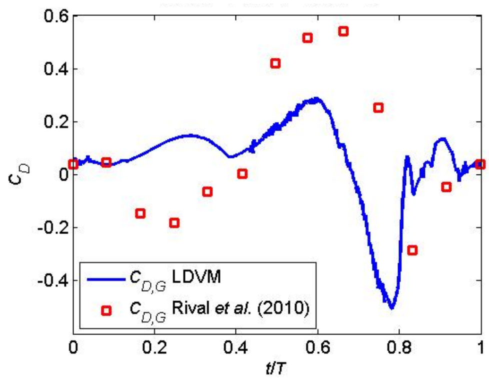

(b)

Fig. 7: Comparison between the global aerodynamic coefficients obtained from PIV measurements and combined control volumes (Rival et al. (2010)) and LDVM for an oscillatique forefoil and a staic hindfoil with an angle of attack of 8°: (a) lift coefficient, (b) drag coefficient.

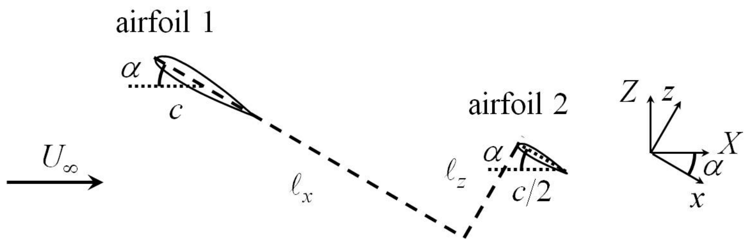

Fig. 8: Two-airfoil arrangement for experimental data from Faure et al. (2017) with chord-wise distance ℓ_x and distance normal to the chord ℓ_z.

foil corresponds to a shadow zone where PIV measurements are impossible. In LDVM simulations (figures 9c and 9d), each LEV or TEV center is represented by a color dot in blue (respectively red) for a clockwise (respectively counter-clockwise) circulation or in green for circulation close to zero. These two time instants have been chosen arbitrary because of the closeness of the shedding vortices, corresponding to clusters of several LEV or TEV centers. Note that the angles of attack and Reynolds numbers are similar, but the airfoils are different (NACA 23012 for experiment and SD7003 for LDVM), which can explain some local discrepancies. That choice is driven by the fact that these two airfoils are cambered airfoils and because the variation of the critical LESP with Reynolds number has been published in Ramesh et al. (2013a). The comparison of the position of shedding vortex structures, for angles of attack $\alpha = 15^\circ$ and $\alpha = 30^\circ$, where both airfoils suction sides are detached, is discussed. For $\alpha = 15^\circ$ (figure 9a), the forefoil suction side is completely detached from the leading edge, a LEV cluster is observed near $X/c = 1.2$ and 2.2 and TEV clusters around 1.8 and 2.9 with some negative vorticity below that latter vortex. The LEV are advected and interact with the hindfoil leading edge, while the TEV path is below the hindfoil pressure side. Some discrepancies are observed in LDVM simulation for $\alpha = 15^\circ$ (figure 9c) with a LEV cluster near $X/c = 0.8$ and TEV clusters located at 1.6 and 3, and a similar behavior around the hindfoil where vortex clusters are advected downstream. Note that the TEV cluster located at $X/c = 3.8$ cannot be observed in the experiment because this region is in the shadow zone. However, most of the vortex clusters shed from the forefoil are passing near the hindfoil pressure side. For $\alpha = 30^\circ$, the similarity between experiments (figure 9b) and LDVM (figure 9d) is much better with the same shape of the leading edge shear layer and a shedding LEV around $X/c = 2$ and TEV clusters around $X/c = 1.2$ and 2.9. For that angle of attack, the shedding cluster of TEV are advected near the leading edge of the hindfoil. Then, a relative agreement is found on time development of the flow between experimental results and LDVM simulations for both of these angles of attack.

In order to get the time-averaged development of the aerodynamic coefficients with angle of attack, comparing the single-airfoil arrangement with the two-airfoil arrangement, let us define the monoplane lift coefficient as (Jones et al. (2015)):

$$C_{L,m} = \frac{S_1 C_{L,1,s} + S_2 C_{L,2,s}}{S_1 + S_2} \tag{34}$$

where $C_{L,1,s}$ and $C_{L,2,s}$ are the lift coefficients for the hindfoil and forefoil in a single-airfoil arrangement and S_1 and S_2 their respective wing areas. Note for the present two-dimensional setup $S_1 = c$ and $S_2 = c/2$. For the two-airfoil arrangement, the total lift coefficient is:

$$C_{L,t} = \frac{S_1 C_{L,1} + S_2 C_{L,2}}{S_1 + S_2} \tag{35}$$

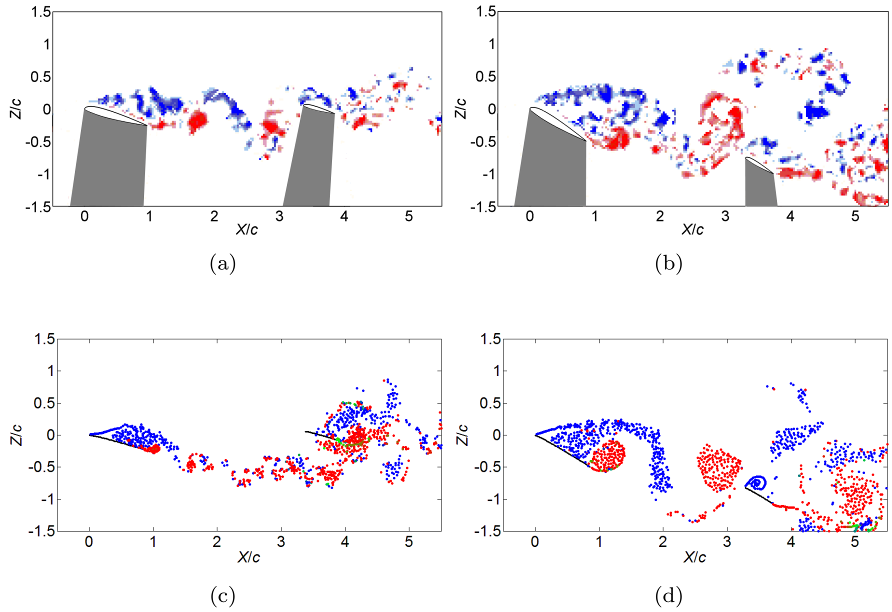

Fig. 9: Vortex shedding for the two-airfoil arrangement with $\ell_x/c = 3$ and $\ell_z/c = 1$ for experimental values of the Γ_2 criterion (negative in blue and positive in red, Faure et al. (2017)) obtained at an angle of attack: (a) $\alpha = 15°$, (b) $\alpha = 30°$, instantaneous LDVM simulations of the circulation centers (negative in blue, close to 0 in green and positive in red) at an angle of attack: (c) $\alpha = 15°$, (d) $\alpha = 30°$.

where $C_{L,1}$ and $C_{L,2}$ are the lift coefficients for the hindfoil and forefoil in the two-airfoil arrangement. Drag and quarter-chord pitching moment coefficients are defined in the same way.

The monoplane and total aerodynamic coefficients versus angle of attack are presented in figures 10 to 12 for NACA 23 012 airfoils with $\ell_x/c = 3$ and $\ell_z/c = 1$ at a Reynolds number of 5.83×10^4 and upstream turbulence level of 0.38% (Faure et al. (2017)), and for present LDVM simulations with the same parameters but SD7003 airfoils. In addition, aerodynamic coefficients are provided for a single-airfoil Wortmann FX63 − 137 at a Reynolds number of 8.5×10^4 and upstream turbulence level of 0.08% (Scharpf and Mueller (1992)) and lift coefficient is given for a single-airfoil 5% camber circular arc with $A_R = 4$ and 6, a Reynolds number of 2.07×10^4 and upstream turbulence level of 0.02% (Laitone (1997)). In the attached flow region, between $-9°$ and $7°$, there is a linear dependence of the lift coefficient and a good agreement between experiments (Faure et al. (2017), Scharpf and Mueller (1992)) and LDVM simulations (figure 10). The slope is lower for experimental results of

Laitone (1997), because of a smaller aspect ratio. Note the stall angles observed in NACA 23 012 airfoils experiments around 7°, below the value of 14° observed in Scharpf and Mueller (1992), probably due to a different airfoil shape but also different wing surface roughness or wind tunnel upstream turbulence levels. LDVM simulations show a stall point around 17°, but no important drop in the lift coefficient is observed after this value. For much larger angle of attack, the lift coefficient is increasing again. The experimental curve for the Wortmann FX63 − 137 airfoil (Scharpf and Mueller (1992)) is close to the monoplace lift coefficent up to the stall angle of 14°. In addition, it has been shown, for angles of attack greater than 25° and for a very low upstream turbulence level of 0.02% (Laitone (1997)), that a change is observed in the lift coefficient curves for aspect ratios shifting from 4 to 6. This behavior is confirmed in figure 10 where the measurements of Laitone (1997) tend to converge toward the monoplane lift coefficient of LDVM simulations, corresponding to a null upstream flow turbulence level and an infinite wing aspect ratio (Faure et al. (2019)). There is no noticeable difference between the monoplane and total lift coefficient for the NACA 23 012 airfoils in the attached flow region between −9° and 7°. However, the two-airfoil arrangement produces experimentally a slightly larger lift coefficient between 8° and 13°, which is not the case for LDVM simulations where the single-airfoil arrangement produces larger values of lift coefficient.

Thus, the advantage of the two-airfoil arrangement seems to be strongly dependent on the range of angle of attack considered, but also the choice of the airfoils and the distance between them. The agreement between LDVM results and experiments is good for the drag coefficient (figure 11) and the quarter-chord pitching moment coefficient (figure 12), even if little dispersion is observed between the plots for angles of attack larger than 20°.

4.2 Parametric study with stagger and gap in the two-airfoil arrangement

In this setting (Scharpf and Mueller (1992), Jones et al. (2015)) the distances are counted in the upstream flow frame of reference (X, Z), defining a gap $\Delta X/c$ and a stagger $\Delta Z/c$ between two airfoils of equal chord c (figure 13). The distance between the forefoil trailing edge and the hindfoil leading edge is modified with the angle of attack. In present LDVM simulations, for comparisons with these experimental data, a SD7003 airfoil is considered again, because the development of LESP$_{crit}$ with Reynolds number is available. In order to find favorable parameters of the two-airfoil arrangement, a parametric study of flow features and lift coefficient is conducted varying the airfoil stagger $\Delta X/c$ and gap $\Delta Z/c$. The LDVM simulations for SD7003 airfoils are compared with experimental results for flat plates (Jones et al. (2015)) at the same Reynolds number of 10^5. Several LDVM simulations have been conducted varying the stagger between 0 and 1.5 and the gap between −1.5 and 1.5 (figures 14 and 15). The monoplane lift coefficient, corresponding to a single-airfoil arrangement, is represented by black squares while the other curves correspond

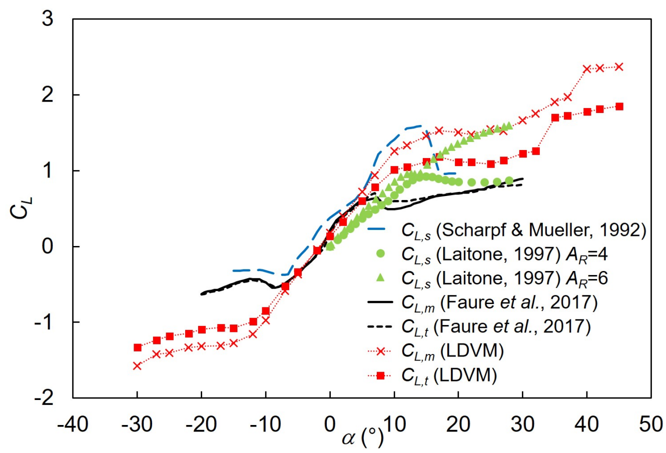

Fig. 10: Lift coefficient versus angle of attack for the single-airfoil arrangement from measurements of Scharpf and Mueller (1992) around a Wortmann FX63−137 airfoil and a Reynolds number of 8.5×10^4, from measurements of Laitone (1997) around a 5% camber circular arc airfoil with $A_R = 4$ and 6 and a Reynolds number of 2.07×10^4, and for the two-airfoil arrangement with $\ell_x/c = 3$ and $\ell_z/c = 1$ from measurements of Faure et al. (2017) around NACA 23 012 airfoils and a Reynolds number of 5.83×10^4 and for LDVM simulations with $\ell_x/c = 3$ and $\ell_z/c = 1$ around SD7003 airfoils and a Reynolds number of 5.83×10^4.

to various values of the gap $\Delta Z/c$, for a given value of the stagger $\Delta X/c$. For seek of clarity, negative and positive gaps are plotted in different figures. In addition, monoplane and total lift coefficients for flat plates are given (figure 14c) from Jones et al. (2015) and for Wortmann FX63 − 137 airfoils (figure 15d) at a different Reynolds number of 8.5×10^4 from Scharpf and Mueller (1992). Note that the LDVM curve for the monoplane lift coefficient is slightly different from the one presented in figure 10 because of the change in Reynolds number.

There is less scatter in the curves for small values of the stagger $\Delta X/c$. For the linear part of the lift coefficient versus angle of attack, corresponding roughly to $\alpha < 10°$ and a slope of 2π rad^{-1} , little discrepancy is observed between the curves, but the monoplane lift coefficient is better. Note, in that region, that the total lift coefficient for the two-airfoil arrangement presents values closer to the ones for the single-airfoil arrangement for larger absolute values of the gap $\Delta Z/c$. A gain in lift coefficient for the two-airfoil arrangement is found between 15° and 35° for particular values of the gap. A maximum gain of 37% is reached for $\Delta X/c = 0$ and $\Delta Z/c$ between 0.5 and 0.75 (figure 14a). For the angles of attack larger than 35°, the monoplane lift coefficient is always larger. Comparing these LDVM simulations with measurements of

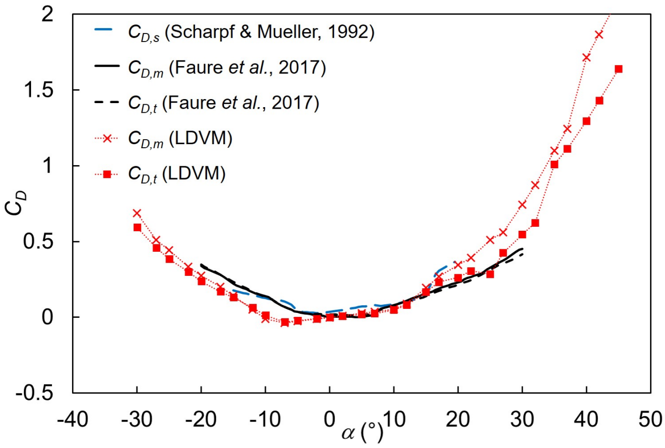

Fig. 11: Drag coefficient versus angle of attack for the single-airfoil arrangement from measurements of Scharpf and Mueller (1992) around a Wortmann FX63 − 137 airfoil and a Reynolds number of 8.5×10^4 and for the two-airfoil arrangement with $\ell_x/c = 3$ and $\ell_z/c = 1$ from measurements of Faure et al. (2017) around NACA 23 012 airfoils and a Reynolds number of 5.83×10^4 and for LDVM simulations with $\ell_x/c = 3$ and $\ell_z/c = 1$ around SD7003 airfoils and a Reynolds number of 5.83×10^4.

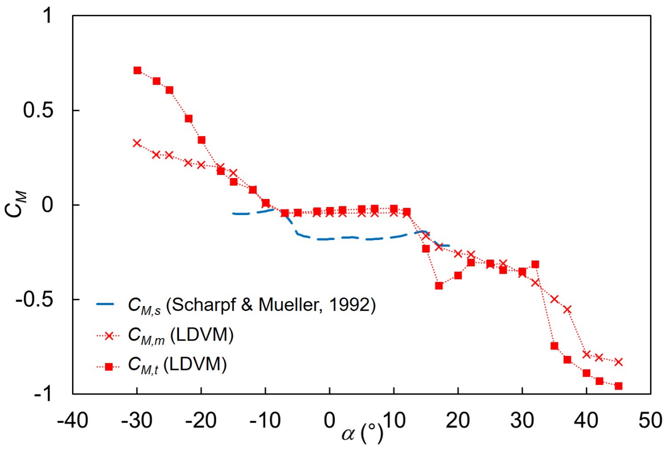

Fig. 12: Quarter-chord pitching moment coefficient versus angle of attack for the single-airfoil arrangement from measurements of Scharpf and Mueller (1992) around a Wortmann FX63 − 137 airfoil and a Reynolds number of 8.5×10^4 and for LDVM simulations with $\ell_x/c = 3$ and $\ell_z/c = 1$ around SD7003 airfoils and a Reynolds number of 5.83×10^4.

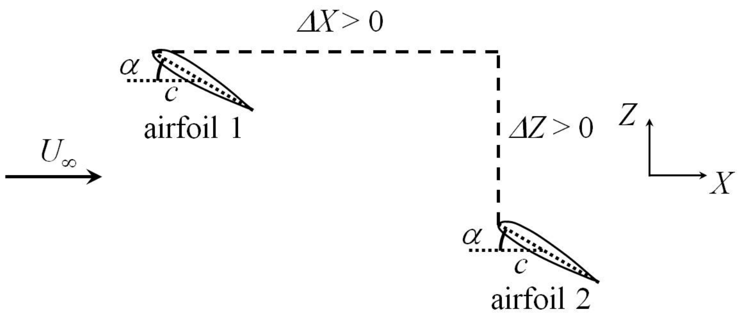

Fig. 13: Two-airfoil arrangement for experimental data from Scharpf and Mueller (1992) and Jones et al. (2015) with stagger ΔX and gap ΔZ in the upstream flow direction.

Jones et al. (2015) on flat plates arrangements at the same Reynolds number and for $\Delta X/c = 0.5$, a lower slope of the attached flow region is observed between 0° and 12° (figure 14c). This is due to the value of 2 for the semi-aspect ratio of the wings, resulting in a lower slope of the lift coefficient (Glauert (1926)), in comparison with present two-dimensional LDVM simulation (infinite aspect ratio). For $12° < \alpha < 30°$, a gain of around 28% is observed for the gaps $\Delta Z/c = 0.85$ and 0.9, which is larger than what is found in present LDVM simulations between $\Delta Z/c = 0.75$ and 1 (around 15%). Comparisons with measurements of Scharpf and Mueller (1992) at a slightly lower Reynolds number of 8.5×10^4 (figure 15d), show a slope of the lift coefficient closer to 2π rad^{-1}. Again, the monoplane lift coefficient is better, up to the post-stall drop for $\alpha > 18°$. LDVM simulation seems to agree relatively well with available experimental data, as far as different airfoils are use for comparison.

5 Lift efficiency ratio

In order to quantify the control induced by potential effects or vortex shedding between the airfoils, a systematic study of the lift coefficient is carried out for different gaps and staggers. The lift efficiency ratio is defined (Jones et al. (2015)), comparing the averaged total lift coefficient for the two-airfoil arrangement $C_{L,t}$ with the averaged monoplane lift coefficient $C_{L,m}$ as:

$$R_L = \frac{C_{L,t}}{C_{L,m}} \tag{36}$$

The comparison of present LDVM simulations with measurements of Scharpf and Mueller (1992) are given in table 1. The agreement of the lift efficiency ratio is relatively good, since airfoils and Reynolds numbers are slightly different, but there is only one arrangement (stagger $\Delta Z/c = 0$ and gap $\Delta X/c = 1.5$)

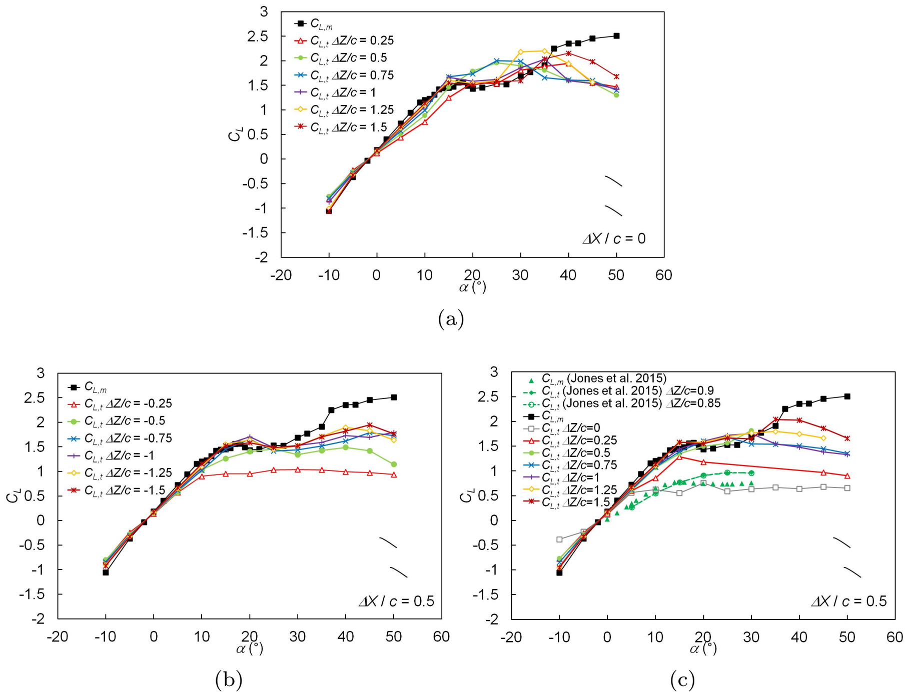

Fig. 14: Lift coefficient obtained by LDVM versus angle of attack for SD7003 airfoils and a Reynolds number of 10^5 for the monoplane arrangement and the two-airfoil arrangement for different values of stagger and gap: (a) $\Delta X/c = 0$, (b) $\Delta X/c = 0.5$ and $\Delta Z/c < 0$, (c) $\Delta X/c = 0.5$ and $\Delta Z/c \geq 0$ with comparisons to a two-plate arrangement of flat plates (Jones et al. (2015)).

and three values of the angle of attack. In order to provide a wider range of comparison, the data of Jones et al. (2015) concerning a two-airfoil arrangement of flat plates is chosen. Note that this airfoil is not cambered, it would provide lower lift coefficient than a cambered airfoil for the same angle of attack, and would promote flow detachment. In addition, the semi-aspect ratio of 2 in Jones et al. (2015) is relatively small in comparison with that of the present two-dimensional LDVM simulations.

Figures 16 and 17 present the lift efficiency ratio versus the angle of attack for a Reynolds number of 10^5, with different stagger $\Delta X/c$ steps, between 0.5 and 1.5 and gap $-1 \leq \Delta Z/c \leq 1.5$. As the comparison between LDVM and measurements is realized between airfoils of different camber and thickness, the data for $\alpha = 5°$ are not plotted, because the low values of lift coefficient for low values of the angle of attack are leading to greater errors in the estimate of lift efficiency ratios. In figure 16a for $\Delta X/c = 0$, an increase of the lift efficiency ratio is obtained for $\Delta Z/c \geq 0.5$. and angles of attack larger than 15°,

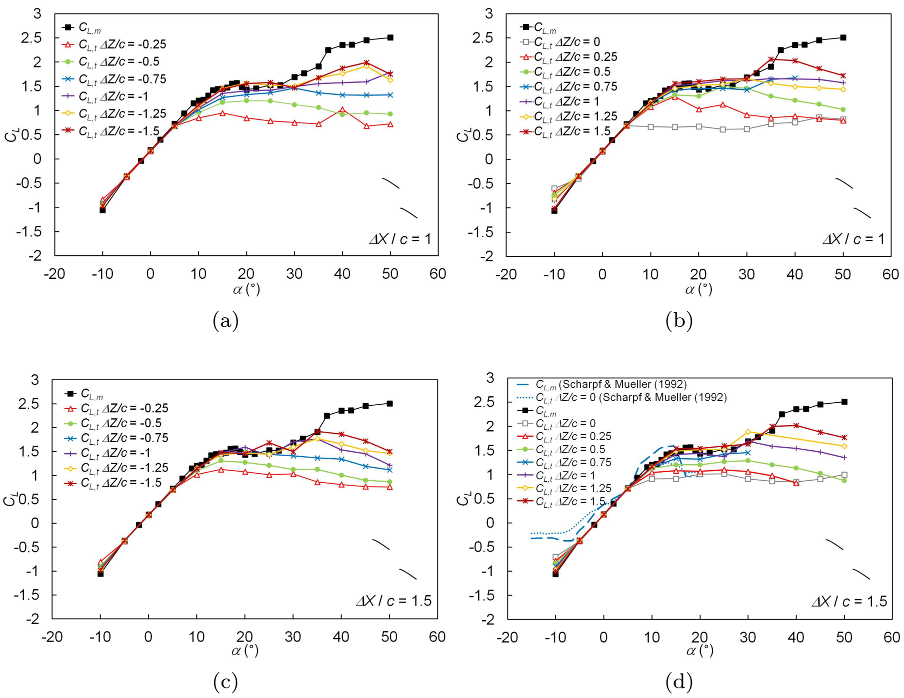

Fig. 15: Lift coefficient obtained by LDVM versus angle of attack for SD7003 airfoils and a Reynolds number of 10^5 for the monoplane arrangement and the two-airfoil arrangement for different values of stagger and gap: (a) $\Delta X/c = 1$ and $\Delta Z/c < 0$, (b) $\Delta X/c = 1$ and $\Delta Z/c \geq 0$, (c) $\Delta X/c = 1.5$ and $\Delta Z/c < 0$, (d) $\Delta X/c = 1.5$ and $\Delta Z/c \geq 0$ with comparisons to a two-airfoil arrangement of Wortmann FX63 $-$ 137 airfoils at a Reynolds number of 8.5×10^4 (Scharpf and Mueller (1992)).

corresponding to detached flow conditions of the single-airfoil arrangement. The maximum gain in lift efficiency is 1.31 for $\Delta Z/c = 0.75$ and $\alpha = 25°$. A similar result is observed for a flat plate arrangement in figure 16b (Jones et al. (2015)), but for angles of attack larger than 20° and with a maximum gain of 1.11 for $\Delta Z/c = 0.83$ and $\alpha = 30°$. For $\Delta X/c = 0.5$, there is a similar development of R_L with gap and angle of attack for both LDVM simulations around SD7003 airfoils (figure 16c) and experiments around flat plates (figure 16d). A minimum value of the lift efficiency, lower than 0.4, is found for $\Delta Z/c = 0$. A gain in efficiency is obtained for $\alpha > 20°$ and $\Delta Z/c \geq 0.5$, with a maximum of 1.13 for SD7003 airfoils and 1.32 for flat plates. Note for the arrangement of SD7003 airfoils, a second region of gain in lift efficiency, which is not much present for the arrangement of flat plates, for $\Delta Z/c \leq -0.5$, with a maximum of 1.19 for $\Delta Z/c = -1$ and $\alpha = 20°$. A similar tendency is observed for stagger

Researchers	Airfoil	α (°)	R_L
Scharpf and Mueller (1992)	Wortmann FX63 − 137	0	0.97
		5	1.00
		10	0.79
present LDVM	SD 7003	0	0.94
		5	0.98
		10	0.76

Table 1: Lift efficiency ratio for stagger $\Delta Z/c = 0$ and gap $\Delta X/c = 1.5$ at angles of attack between 0° and 10° and for a two-airfoil arrangement of Wortmann FX63−137 at a Reynolds number of 8.5×10^4 (experimental results, Scharpf and Mueller (1992)) and for a two-airfoil arrangement of SD7003 at a Reynolds number of 10^5 (present LDVM).

$\Delta X/c = 1.5$ with a maximum gain of 1.12 for SD7003 airfoils (figure 17a) and 1.26 for flat plates (figure 17b), and a gain of 1.09 for SD7003 airfoils and $\Delta Z/c = -1.25$. Again, the same tendency is found for $\Delta X/c = 1.5$, with a maximum gain of 1.12 for SD7003 airfoils (figure 17c), a slight decrease of the gain of 1.15 for flat plates (figure 17d), and a gain of 1.11 for SD7003 airfoils and $\Delta Z/c = -1$. A general agreement is found between LDVM and the experiment, although the airfoils and wing aspect ratios considered are different.

Figure 18 presents the flow vortices for stagger $\Delta X/c = 1$ and angle of attack $\alpha = 20°$ for the single-airfoil arrangement and the two-airfoil arrangement, with different gaps $\Delta Z/c$ at the same time of the simulation. The value of the angle of attack corresponds to the maximum lift efficiency ratio obtained for $|\Delta Z/c| \geq 0.75$. The reference of the single-airfoil arrangement is presented in figure 18a. A detached flow starts from the leading edge of the airfoil, evidenced by the generation of a shear layer consisting in a line of negative circulation centers. These centers merge into a large vortical structure on the suction side. For this particular time, a LEV is about to leave the detached airfoil. We can also observe the generation of a TEV and the development of a wake with pairs of counter-rotating shedding vortex clusters. For the two-airfoil arrangement and $\Delta Z/c = -1.5$ (figure 18b), a potential interaction between the airfoils is evidenced by discrepancies in vortex clusters generation from the single-airfoil arrangement. In particular, a large vortex structure is forming on the suction side of the forefoil, with a mixing of positive and negative vortical centers shedding downstream. This is the evidence of a phase shift of the vortex shedding between the two airfoils. The gain in R_L observed for this value of gap is probably due to a potential effect between the bound circulation of the airfoils. Similar flow features are observed for $\Delta Z/c = -1$

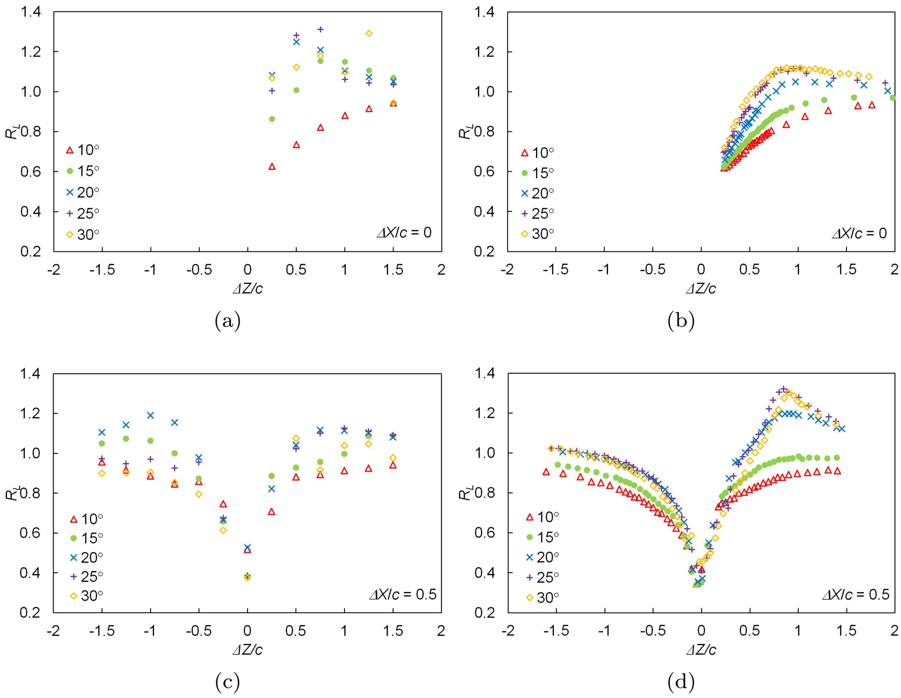

Fig. 16: Lift efficiency ratio versus gap $\Delta Z/c$ for a two-airfoil arrangement at a Reynolds number of 10^5: left column LDVM results of SD7003 airfoils for: (a) $\Delta X/c = 0$, (c) $\Delta X/c = 0.5$, right column experimental results of flat plates (Jones et al. (2015)) for: (b) $\Delta X/c = 0$, (d) $\Delta X/c = 0.5$.

(figure 18c), with no mixing between the LEV and TEV emitted from the two airfoils in the wake. For $\Delta Z/c = -0.5$ (figure 18d), the airfoils closeness strongly affects vortex shedding. The detached flow region on the forefoil is deviated above by the hindfoil, resulting in a drop of the total lift coefficient as observed in figure 17b. For $\Delta Z/c = 0$ (figure 18e), the LEV and TEV of the forefoil are trapped between the two airfoils, resulting in a very strong interaction, a detached pressure side on the hindfoil and a single wake and vortex shedding. As a consequence, the lift coefficient on each airfoil is half the one obtained for a single-airfoil arrangement, resulting in $R_L \sim 0.5$ (figure 17a). For $\Delta Z/c = 0.5$ (figure 18f), for the particular value of stagger $\Delta X/c = 1$, the two airfoils are practically aligned and form an unique airfoil, resulting in an attached pressure side and a completely detached suction side. The flow on this airfoil arrangement is rather similar to the flow around a single airfoil of chord $2c$ and as a result $R_L \sim 1$ (figure 17a). A unique wake, consisting in pairs of counter-rotating vortices, is developing downstream. The interaction between the shedding vortices from the forefoil and hindfoil suction sides be-

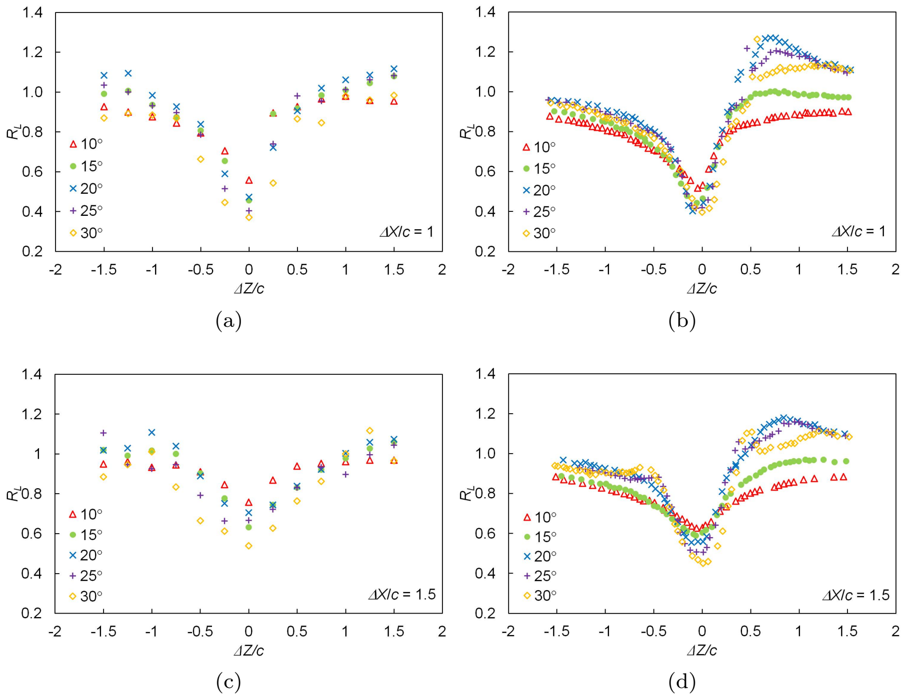

Fig. 17: Lift efficiency ratio versus gap $\Delta Z/c$ for a two-airfoil arrangement at a Reynolds number of 10^5: left column LDVM results of SD7003 airfoils for: (a) $\Delta X/c = 1$, (c) $\Delta X/c = 1.5$, right column experimental results of flat plates (Jones et al. (2015)) for: (b) $\Delta X/c = 1$, (d) $\Delta X/c = 1.5$.

comes positive again for $\Delta Z/c = 1$ (figure 18g). For particular times, the LEV of the forefoil is forcing the reattachment of the flow on the hindfoil pressure side, leading to $R_L > 1$. Similar features are observed for $\Delta Z/c = 1.5$ (figure 18h). Note that in these two arrangements, two distinct wakes with pairs of counter-rotating vortices, are developing downstream from the airfoils.

In order to understand the positive interaction between the airfoils, figure 19 presents vortex shedding for stagger $\Delta X/c = 1$, gap $\Delta Z/c = 1$ and $\alpha = 20^\circ$ for three different times, for which the flow is completely established. A detached flow is continuously starting from the leading edge of the forefoil. These centers of negative vorticity can merge into a large vortical structure on the suction side. The potential effect between the airfoils and the shedding vortices influence on them, are clearly observed by an asymmetry of the vortical centers flowing around each airfoil. In particular the LEV shedding from the forefoil on the hindfoil suction side produces a leading edge reattachment at some time (figure 19a). The suction side of the hindfoil is also able to detach from the leading edge and generate a LEV (figure 19b). The consequence of

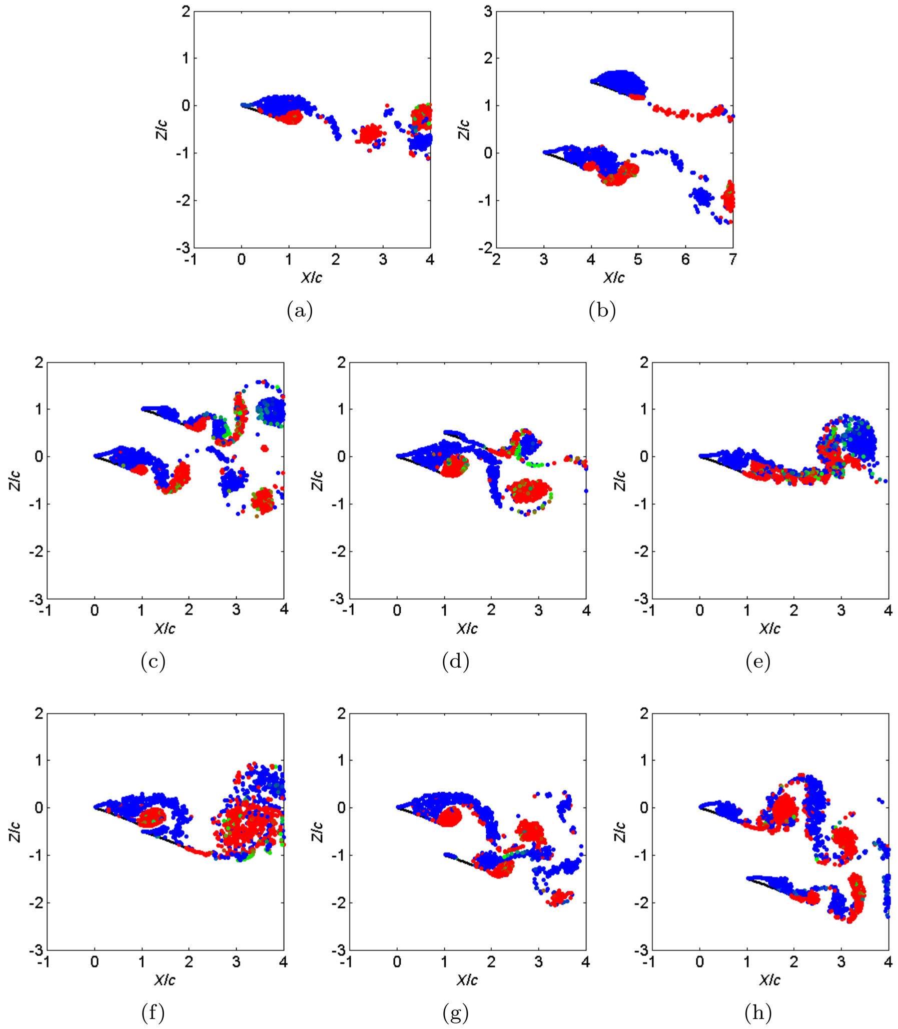

Fig. 18: Vortex shedding (vortex circulation negative in blue, close to 0 in green and positive in red) at 20° angle of attack for $t^* = 100$ for: (*a*) a single-airfoil arrangement, and for the two-airfoil arrangement for stagger $\Delta X/c = 1$ and gap: (*b*) $\Delta Z/c = -1.5$, (*c*) $\Delta Z/c = -1$, (*d*) $\Delta Z/c = -0.5$, (*e*) $\Delta Z/c = 0$, (*f*) $\Delta Z/c = 0.5$, (*g*) $\Delta Z/c = 1$, (*h*) $\Delta Z/c = 1.5$.

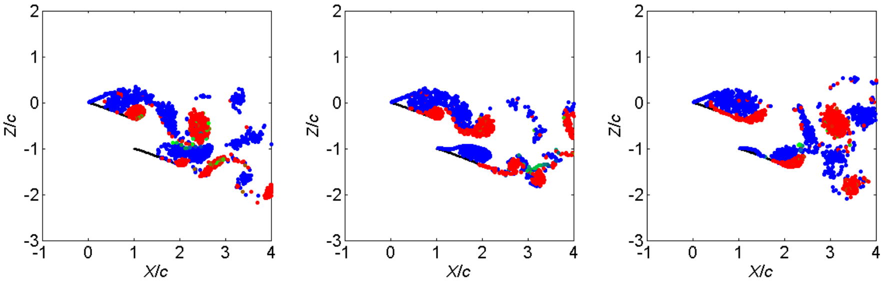

(a) (b) (c)

Fig. 19: Vortex shedding (vortex circulation negative in blue, close to 0 in green and positive in red) for a two-airfoil arrangement with SD7003 airfoils at a Reynolds number of 10^5 for stagger $\Delta X/c = 1$, gap $\Delta Z/c = 1$ and $\alpha = 20^{\circ}$ for different times of the simulation.

alternate detached and attached flow on the suction side of the hindfoil is a time-averaged total lift coefficient larger than the monoplane coefficient for the same airfoil and angle of attack. This mechanism can be interpreted as a flow forcing, or passive control, of the suction side of the hindfoil by the vortex structures shedding from the forefoil. LEV and TEV from the forefoil and fhindfoil are mixing in the wake resulting in the two-airfoil arrangement with two pairs of counter-rotating shedding vortices (figure 19c).

Figures 20 and 21 show the lift coefficient for the individual airfoils as a function of gap $\Delta Z/c$ for $\alpha = 20^{\circ}$. The dashed line corresponds to the monoplane lift coefficient and the green squares to the total lift coefficient. For $\Delta X/c = 0$ (figure 20a) the upper forefoil produces greater lift than the lower forefoil, except for $\Delta Z/c = 0.25$ where the two airfoils are very close. The upper airfoil forces the flow over the lower airfoil closer to the surface, producing for this latter airfoil a reattachment of the separated shear layer from the leading edge and a larger lift coefficient. For $\Delta Z/c = 0.25$, there is a strong high speed flow in the region between the airfoils, associated with low pressure resulting in suction on the lower airfoil which would explain the gain in lower airfoil lift and the loss in upper airfoil (Jones et al. (2015)). For $\Delta X/c = 0.5$ (figure 20b), the forefoil produces greater lift than the hindfoil for $\Delta Z/c > -0.5$, the situation is reversed for $\Delta Z/c < -0.5$ and both airfoils produce almost the same lift for $\Delta Z/c = -0.5$. The comparison of the lift coefficients of the forefoil and hindfoil with Jones et al. (2015) for the same stagger but $\alpha = 25^{\circ}$, are rather similar, but the lift on the hindfoil is lower for $\Delta Z/c < 0$. This can be explained by the fact that in present LDVM simulations, a cambered SD7003 airfoil with a round leading edge is considered. For airfoils in close neighborhood, the surface camber and leading edge radius provide a better flow streamlining than a flat plate and better aerodynamic performances. For

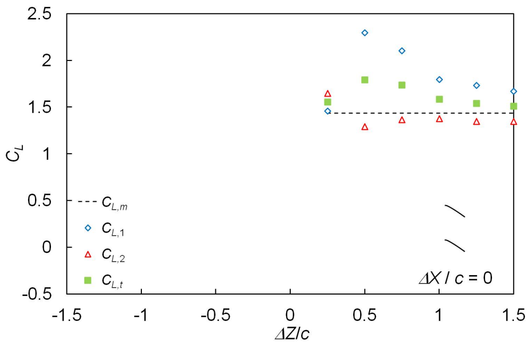

(a)

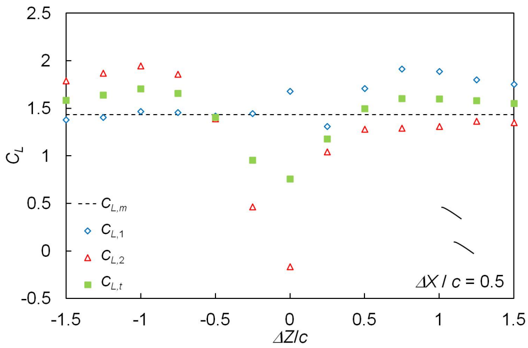

(b)

Fig. 20: Lift coefficient for the single-airfoil and the two-airfoil arrangements at 20° angle of attack versus gap $\Delta Z/c$ for different stagger: (a) $\Delta X/c = 0$, (b) $\Delta X/c = 0.5$.

$\Delta X/c = 1$ and $\Delta X/c = 1.5$ (figures 21a and 21b), similar lift distribution are found between the forefoil and hindfoil than for $\Delta X/c = 0.5$. Note a good agreement with Jones et al. (2015) for these parameters, showing that there is less influence of the airfoil geometry on the flow for large values of the stagger.

6 Conclusion

The LDVM is a useful low-order method to study the instantaneous flow development around an unsteady airfoil at a low computing cost (Ramesh et al. (2014), Faure et al. (2019)). The LDVM is implemented for the investigation of the unsteady flow around a two-airfoil arrangement. To solve the problem, an additional condition is necessary, that is the initial circulation for each airfoil equals zero, while the global flow depends on the whole set of shedding vortices. The two-airfoil LDVM is successively compared to CFD simulations of

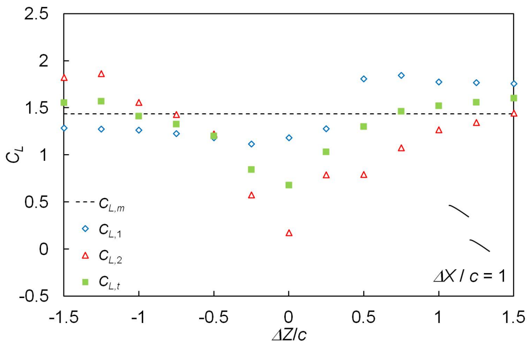

(a)

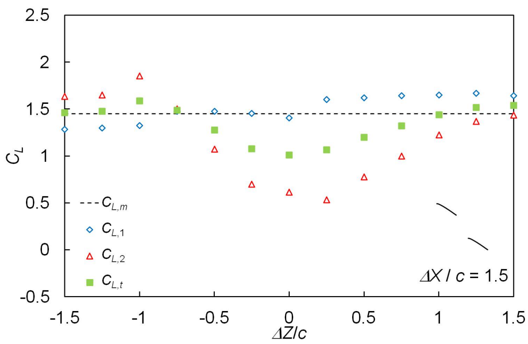

(b)

Fig. 21: Lift coefficient for the single-airfoil and the two-airfoil arrangements at 20° angle of attack versus gap $\Delta Z/c$ for different stagger: (a) $\Delta X/c = 1$, (b) $\Delta X/c = 1.5$.

Broering and Lian (2012) for flapping tandem flat plates at a Reynolds number of 5000 and to PIV measurements of Rival et al. (2010) for the flapping of a SD7003 airfoil on a downstream airfoil at a Reynolds number of 30, 000.

For constant angle of attack static two-airfoil arrangement and fixed distance in airfoil frame of reference, the comparison of instantaneous measured flow fields with LDVM results are in relatively good agreement. The lift, drag and quarter chord pitching moment coefficients agree relatively well, even if some discrepancies in the stall angle values are found, probably due to the difference between the airfoils under comparison, aspect ratios and wing surface roughness in the experimental set-up. A parametric study with stagger and gap in the two-airfoil arrangement is carried out for the lift coefficient development with angle of attack. A gain in lift coefficient for the two-airfoil arrangement is found between 15° and 35° for particular values of the gap. A maximum gain is reached for $\Delta X/c = 0$ and $\Delta Z/c$ between 0.5 and 0.75. For the angles of attack larger than 35°, the monoplane lift coefficient is always larger. In order to find the best arrangement between the airfoils, a lift efficiency ratio is defined comparing the averaged total lift coefficient for the two-airfoil arrangement with the monoplane lift coefficient. Comparison of the present LDVM simulations on an arrangement of two SD7003 airfoils with the measurements obtained on a two-plate arrangement are in very good agreement in terms of the development of the lift efficiency ratio with angle of attack and gap. Minima of the lift efficiency ratio are observed for small gaps $\Delta Z/c \sim 0$, and maxima for large gaps and large angles of attack, typically larger than 20°. Because of the relatively low values of the maximum lift coefficient observed for the two-plate arrangement, the lift efficiency ratio is better than for the two-airfoil arrangement. In addition, a second region of gain in the lift efficiency ratio is found for the two-airfoil arrangement for negative values of the gap, which is not really found for the two-plate arrangement. This is evidence that the airfoil camber and leading edge curvature radius must contribute to the efficiency improvement of the arrangement. The physical analysis of the lift efficiency gain is studied from vortex shedding from LDVM simulations arrangement of two SD7003 airfoils. For large values of the gap, typically $|\Delta Z/c| > 1$, the lift efficiency gain is mainly caused by a potential interaction between the bound circulation of the airfoils. For small values of the gap, the vortices shedding from the forefoil are trapped and cause a detachment on the hindfoil pressure side and a drop of the lift coefficient. A vortex forcing of the suction side of the hindfoil by vortices shedding from the forefoil at particular times is also observed for $\Delta Z/c = 1$, resulting in an increased lift efficiency ratio.

The two-airfoil arrangement seems to be a good way of improving airfoil lift performances for detached flow conditions and particular setting of the stagger and gap. This result is valid for cambered airfoils as for flat plates. The LDVM algorithm adapted to that configuration has proved to be a rapid and useful tool for aerodynamic coefficient prediction and flow analysis.

References

Ansari SA, Zbikowski R, Knowles K (2006) A nonlinear unsteady aerodynamic model for insect-like flapping wings in the hover. Part 2: implementation and validation. Proceedings of the Institution of Mechanical Engineers, Part G: Journal of Aerospace Engineering 30(2):169–186

Barnes J, Hut P (1986) A hierarchical O(NlogN) force-calculation algorithm. Nature 324:446–449

Bentley JL (1975) Multidimensional binary search trees used for associative searching. Communications of the ACM 18(9):509–517

Birnbaum W (1923) Die tragende Wirbelfläche als Hilfsmittel zur Behandlung des ebenen Problems der Tragflügeltheorie. ZAMM-Journal of Applied Mathematics and Mechanics/Zeitschrift für Angewandte Mathematik und Mechanik 3(4):290–297

Broering T, Lian Y (2012) The effect of phase angle and wing spacing on tandem flapping wings. Acta Mechanica Sinica 28(6):1557–1571

Carrier J, Greengard L, Rokhlin V (1988) A fast adaptative multipole algorithm for particle simulations. SIAM Journal of Computational Physics 9(4):5628–5649

Clements RR (1973) An inviscid model of two-dimensional vortex shedding. Journal of Fluid Mechanics 57(2):321–336

Clements RR, Maull DJ (1975) The representation of sheets of vorticity by discrete vortices. Progress in Aerospace Science 16(2):129–146

Crowdy D (2007) Schwarz–christoffel mappings to unbounded multiply connected polygonal regions. In: Mathematical Proceedings of the Cambridge Philosophical Society, Cambridge University Press, vol 142, pp 319–339

Crowdy D (2008) The schwarz problem in multiply connected domains and the schottky–klein prime function. Complex Variables and Elliptic Equations 53(3):221–236

Crowdy D (2010) A new calculus for two-dimensional vortex dynamics. Theoretical and Computational Fluid Dynamics 24(1-4):9–24

Crowdy D, Marshall J (2006) Conformal mappings between canonical multiply connected domains. Computational Methods and Function Theory 6(1):59–76

Crowdy D, Surana A (2007) Contour dynamics in complex domains. Journal of Fluid Mechanics 593:235–254

Crowdy D, Surana A, Yick K (2007) The irrotational motion generated by two planar stirrers in inviscid fluid. Physics of Fluids 19(1):018103

Darakananda D, Eldredge JD (2019) A versatile taxonomy of low-dimensional vortex models for unsteady aerodynamics. Journal of Fluid Mechanics 858:917–948

Darakananda D, de Castro da Silva A, Colonius T, Eldredge J (2018) Data-assimilated low-order vortex modeling of separated flow. Physical Review Fluids 3:124701

Faure TM, Hétru L, Montagnier O (2017) Aerodynamic features of a two-airfoil arrangement. Experiments in Fluids 58(10):146

Faure TM, Dumas L, Drouet V, Montagnier O (2019) A modified discrete-vortex method algorithm with shedding criterion for aerodynamic coefficients prediction at high angle of attack. Applied Mathematical Modelling 69:32–46

Garrick IE (1937) Propulsion of a flapping and oscillating airfoil. Tech. rep., NACA TN-D-85

Glauert H (1926) The elements of aerofoil and airscrew theory. Cambridge University Press

Graftieaux L, Michard M, Grosjean N (2001) Combining PIV, POD and vortex identification algorithms for the study of unsteady turbulent swirling flows. Measurement Science and Technology 12(9):1422

Hammer P, Altman A, Eastep F (2014) Validation of a discrete vortex method for low Reynolds number unsteady flow. AIAA journal 52(3):643–649

Jones R, Cleaver D, Gursul I (2015) Aerodynamics of biplane and tandem wings at low Reynolds numbers. Experiments in Fluids 56(124)
von Kármán T, Sears W (1938) Aerofoil theory for non-uniform motion. Journal of Aeronautical Science 5(10):379–390
Katz J (1981) Discrete vortex method for the the non-steady separated flow over an aerofoil. Journal of Fluid Mechanics 102:315–328
Katz J, Plotkin A (2001) Low-Speed Aerodynamics. Cambridge University Press
Kiya M, Arie M (1977) A contribution to an inviscid vortex-shedding model for an inclined flat plate in uniform flow. Journal of Fluid Mechanics 82(2):241–253
Kuwahara K (1973) Numerical study of flow past an inclined flat plate by an inviscid model. Journal of the Physical Society of Japan 35:1545
Laitone EV (1997) Wind tunnel tests of wings at Reynolds numbers below 70 000. Experiments in Fluids 23(5):405–409
Leonard A (1980) Vortex methods for flow simulation. Journal of Computational Physics 37(3):289–335
Lighthill M (1973) On the weis-fogh mechanism of lift generation. Journal of Fluid Mechanics 60(1):1–17
Michelin S, Smith SGL (2009) An unsteady point vortex method for coupled fluid–solid problems. Theoretical and Computational Fluid Dynamics 23(2):127–153
Mueller TJ, DeLaurier JD (2003) Aerodynamics of small vehicles. Annual Review of Fluid Mechanics 35(1):89–111
Munk M (1922) General theory of thin wing sections. Tech. rep., 142 NACA
Ramesh K (2013) Theory and low-order modeling of unsteady airfoil flows. PhD thesis, North Carolina State University, Rayleigh, NC, USA
Ramesh K, Gopalarathnam A, Ol MV, Granlund K, Edwards JR (2011) Augmentation of inviscid airfoil theory to predict and model 2d unsteady vortex dominated flows. In: 41st AIAA Fluid Dynamics Conference and Exhibit, Honolulu, Hawai, USA, AIAA Paper 2011-3578
Ramesh K, Gopalarathnam A, Edwards J, Granlund K, Ol M (2013a) Theoretical analysis of perching and hovering maneuvers. In: 31st AIAA Applied Aerodynamics Conference, p 3194
Ramesh K, Gopalarathnam A, Edwards JR, Ol MV, Granlund K (2013b) An unsteady airfoil theory applied to pitching motions validated against experiments and computation. Theoretical and Computational Fluid Dynamics 27(6):843–864
Ramesh K, Gopalarathnam A, Granlund K, Ol MV, Edwards JR (2014) Discrete-vortex method with novel shedding criterion for unsteady aerofoil flows with intermittent leading-edge vortex shedding. Journal of Fluid Mechanics 751:500–538
Ramesh K, Granlund K, Ol MV, Gopalarathnam A, Edwards JR (2018) Leading-edge flow criticality as a governing factor in leading-edge vortex initiation in unsteady airfoil flows. Theoretical and Computational Fluid Dynamics 32(2):109–136

Rival D, Manejev R, Tropea C (2010) Measurement of parallel blade-vortex interaction at low reynolds numbers. Experiments in Fluids 49:89–99

Sarpkaya T (1975) An inviscid model of two-dimensional vortex shedding for transient and asymptotically steady separated flow over an inclined plate. Journal of Fluid Mechanics 68(1):109–128

Scharpf DF, Mueller TJ (1992) Experimental study of a low Reynolds number tandem airfoil configuration. Journal of Aircraft 29(2):231–236

Schmidt W (1965) Der Wellpropeller, ein neuer Antrieb fuer Wasserland und Luftfahrzeuge. Z Flugwiss Weltraumforsch 13(12):472–479

SureshBabu AV, Ramesh K, Gopalarathnam A (2016) Model reduction in discrete-vortex methods for 2D unsteady aerodynamic flows. In: 34th AIAA Applied Aerodynamics Conference, AIAA Paper 2016-4163

Theodorsen T (1935) General theory of aerodynamic instability and the mechanism of flutter. Tech. rep., 496 NACA

Vatistas GH, Kozel V, Mih WC (1991) A simpler model for concentrated vortices. Experiments in Fluids 11(1):73–76

Wagner H (1925) Über die Entstehung des dynamischen Auftriebes von Tragflügeln. Z Angew Math Mech 5(1):17–35

Wang C, Eldredge JD (2013) Low-order phenomenological modelling of leading-edge vortex formation. Theoretical Computational Fluid Dynamics 27(5):577–598

Weis-Fogh T (1973) Quick estimates of flight fitness in hovering animals, including novel mechanisms for lift production. Journal of Experimental Biology 59:169–230

Xia X, Mohseni K (2013) Lift evaluation of a two-dimensional pitching flat plate. Physics of Fluids 25:091901